Technische Universität München
Department of Electrical Engineering and Information Technology
Bio-Inspired Information Processing

Master thesis

Implementation and evaluation of biophysical auditory nerve fiber models

Richard Bachmaier

Date of Submission:
February 19, 2019

Supervisors:
Prof. Dr.-Ing. Werner Hemmert
Dr. Siwei Bai
Jörg Enke

Abstract

Computational models are valuable to enhance our understanding how the auditory system encodes acoustical and electrical stimuli. This thesis regards the electrical stimulation of biophysical models of the auditory nerve fiber (ANF). Seven existing ANF models have been implemented and evaluated. In the first step major characteristics of single ANFs were measured and compared with experimentally obtained data. This includes the conduction velocity, thresholds, action potential (AP) shape and latency, stochastic properties, the refractory behavior and pulse train responses. In the second step, spiking patterns of 400 ANFs, stimulated with a 3D model of the implanted human cochlea, were investigated with four of the models.

The measured single ANF characteristics differed considerably among models. None of the models was capable of predicting all characteristics within the experimental range. The results for single pulse stimulation usually compared well with experimental data, but the models could not appropriately account for temporal effects as pulse-train integration or adaptation. The spiking patterns obtained for a stimulation of the ANF model populations suggested an excitation of ANFs across neighboring turns of the cochlea and revealed differences between basal and apical regions.

Acknowledgments

Firstly, I would like to thank Prof. Dr. Werner Hemmert, the head of our group, for the opportunity to write this thesis and his very helpful ideas and suggestions. I would also like to thank my supervisor Siwei Bai for continuously supporting my work with his great knowledge, advises and feedback. Furthermore I really appreciate the helpfulness and kindness of all group members who aided my work in every possible way. Special thanks goes to Jörg Enke and Miguel Obando who contributed a lot to the outcomes of my thesis by helping me with their expertise and many inspiring discussions. Finally, I must express my very profound gratitude to my parents and to my girlfriend for encouraging and supporting me through the years of study. Thank you!

Contents

1 Introduction **1**

2 Model description **3**
2.1 Model overview 3
2.2 Morphology 5
2.3 Electrical equivalent circuits 6
2.4 Ion currents, channel types and gating properties 10
2.5 Adaptation and accommodation 17
2.6 Inclusion of stochasticity 18

3 Implementation **20**

4 Comparison of model characteristics **22**
4.1 Single Fiber characteristics 22
4.1.1 Thresholds 22
4.1.2 Conduction velocity 27
4.1.3 Action potential shape 30
4.1.4 Latency 34
4.1.5 Refractory properties 34
4.1.6 Stochastic properties 39
4.1.7 Pulse-train responses and adaptation 41
4.2 ANF populations 43
4.2.1 Dynamic ranges 44
4.2.2 Spiking patterns 45
4.2.3 Latency 50

5 Summary **51**

6 Outlook **54**

List of Figures **60**

List of Tables **61**

References **69**

Chapter 1

Introduction

Cochlear implants (CIs) are prosthetic devices, which have become successful in restoring partial hearing in deaf and profoundly hearing impaired by converting acoustic vibrations into electrical stimuli. Although their performance in providing speech perception improved a lot over the last decades, there are still limitations. CI users show difficulties in binaural hearing, pitch and music perception and in understanding speech in noise situations (Limb and Roy, 2014; Rubinstein, 2004). Therefore new sound coding and stimulation strategies are developed and tested. As investigations in psychophysical experiments are very time-consuming and performance varies a lot among subjects, computational models of the auditory system can be a valuable tool to evaluate new strategies and help to understand how timing, frequency and intensity information are encoded (Imennov and Rubinstein, 2009).

While the main functionality of the outer, middle and inner ear to collect, transmit and convert acoustic stimuli can be replaced by a CI, the presence of a functioning auditory nerve is crucial for hearing. Hence the primary objective of this thesis is the implementation and comparison of various auditory nerve fiber (ANF) models. Several phenomenological and biophysical approaches have been published in the last decades (Takanen et al., 2016; O'Brien and Rubinstein, 2016). However, considerations here are confined to biophysical models as the use of anatomically and physiologically motivated parameters allows a deeper understanding of their influence on the excitation process.

Chapter 2 gives an overview of the biophysical ANF models in the literature. A selection of seven models, implemented in this work, is discussed in detail. This includes a description of their morphologic structures, equivalent circuits, channel types and gating properties. Furthermore methods to include adaptation and stochasticity are pointed out. Information about the implementation of the ANF models and necessary adaptations of the published model versions can be found in Chapter 3. Major characteristics of the ANF models were measured using a battery of tests and described in Chapter 4. In a first step, properties of single fibers, stimulated with a point electrode, were considered. In a second step, the spiking behavior of 400 ANFs was investigated. These were stimulated with the potential data acquired from a 3D model of the implanted human cochlea. The characteristics of all models were compared with each other as well as with experimentally obtained data, including measurements from animal experiments and CI listeners. Chapter 5 summarizes the results of the thesis and points out the limitations of the models. The last chapter provides an outlook on possible improvements of the ANF models and further tests to be applied in future.

Chapter 2

Model description

2.1 Model overview

The first approaches to simulate nerve fiber responses to electrical stimulation have been single compartment models. The fundamental model was published by Hodgkin and Huxley (1952) who created a biophysical description of a patch of membrane by fitting parameters to voltage clamp measurements on the unmyelinated giant axon of a squid. In the following decades, further membrane models were created based on experiments on toads (Frankenhaeuser and Huxley, 1964), rabbits (Chiu et al., 1979; Sweeney et al., 1987), rats and cats (Schwarz and Eikhof, 1987). Among these, however, only the model of Hodgkin and Huxley (HH) was able to replicate certain phenomena of cochlear implant stimulation and gave the best fit to the observed temporal behavior of ANFs (Motz and Rattay, 1986; Rattay and Aberham, 1993). Therefore contemporary models still follow the equations and parameters of the warm (gating processes accelerated) HH model and they have been extended to multicompartment models of the ANF.

There is little experimental data on human ANFs, since invasive methods like voltage-clamp measurements are not feasible in humans. In contrast, properties of the feline ANF have been studied extensively (Hartmann et al., 1984a; Liberman and Oliver, 1984; Brown and Abbas, 1990). Out of this reason, most models were designed to match with morphological and physiological data from cat measurements and optimized to compare well with the corresponding response behavior. They are considered as feline ANF models, accordingly. Later, differences in the geometry and degree of myelination between human and feline ANFs have been described (Rattay et al., 2001). Thus some modelers used a morphology following a human ANF. Others simplified the morphologic structure by removing the dendrite and soma and created axon models. Seven of the existing biophysical ANF models have been implemented in this thesis.

Table 2.1 – Overview of models implemented in this study.

Authors (Year)	Model type
Rattay et al. (2001)	human ANF
Frijns et al. (1994)	axon
Briaire and Frijns (2005)	human ANF
Smit et al. (2009)	axon
Smit et al. (2010)	human ANF
Imennov and Rubinstein (2009)	axon
Negm and Bruce (2014)	single node

Rattay et al. (2001) published both a feline and a human ANF model. As these merely differ in some morphologic parameters, only the human ANF model was implemented in this study. The earliest model included in the thesis is an axon model by Frijns et al. (1994). It was subsequently extended to follow the feline ANF morphology (Frijns et al., 1995) and then the human one (Briaire and Frijns, 2005). To investigate the impact of a complex morphologic structure, both the simple axon model and the human ANF model were implemented and compared in this work. Smit et al. (2009) published an axon model, which was also upgraded with the human ANF morphology (Smit et al., 2010). Both versions were considered in this thesis. Furthermore the axon model by Imennov and Rubinstein (2009) and the model of a single node of Ranvier by Negm and Bruce (2014) have been implemented. The node model was included due to its promising approach to account for the effects of adaptation, detailed in Sec. 2.5.

Table 2.1 lists the biophysical ANF models, which attracted the widest attention. Further approaches are usually referred to one of the listed models and do not include new concepts (Intyre et al., 2001; Nogueira and Ashida, 2018). The feline ANF model of Woo et al. (2010) is worth to be mentioned, though. It contains an algorithm to model adaptation based on the idea of a dynamic external potassium concentration $[K^+]_e$. However, such changes of $[K^+]_e$ could not be evidenced in experiments, so the model of Woo et al. (2010) was not implemented for the purpose of this thesis.

The following sections describe and compare the methods, that were used in the mentioned models. This includes, among other things, the respective morphologic structures, equivalent circuits and channel types. Basic concepts, shared by all ANF models, are only explained in detail for the model of Rattay et al. (2001).

2.2 Morphology

The ANF models are multicompartment models where the compartments are connected electrical equivalent circuits of the morphological components of a fiber. The structures of the equivalent circuit will be detailed in Sec. 2.3.

Rattay et al. (2001)

All human ANF models implemented in this thesis have a similar basic structure. They consist of a dendrite and an axon, which are the peripheral and central part of the nerve fiber, respectively as well as a soma in between. Dendrite and axon are composed of an alternating structure of nodes of Ranvier and myelinated internodes.

The model of Rattay et al. (2001) also includes a peripheral terminal and a pre- and postsomatic region. The dendrite has a diameter of 1 µm and six internodes, which are shielded by 40 myelin layers. Both the fiber diameter and the degree of myelination are increased by a factor of two for the axon. The soma is spherical and covered by three layers of satellite cells, which have the same isolating properties as myelin layers.

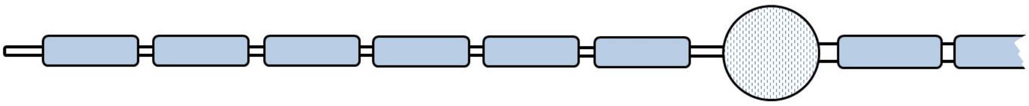

Figure 2.1 – Scheme of the human ANF morphology as used by Rattay et al. (2001). The blue color denotes myelinated components.

As previously mentioned, Rattay et al. (2001) also published a feline ANF model version with a different morphologic structure according to the findings of Liberman and Oliver (1984). It has only three dendritic internodes and no pre- and postsomatic regions. Nodes and internodes are shorter than in the human ANF model and the soma is smaller and myelinated.

Smit et al. (2010)

The morphology of the human ANF model by Smit et al. (2010) is similar to the one as used by Rattay et al. (2001). However, it has only five dendritic internodes and a slightly smaller soma. Furthermore, the axonal internodes are very short compared to other ANF models.

Briaire and Frijns (2005)

The human ANF model of Briaire and Frijns (2005) has six dendritic internodes and a cylindrical soma, surrounded by nodes. The fiber has a constant inner

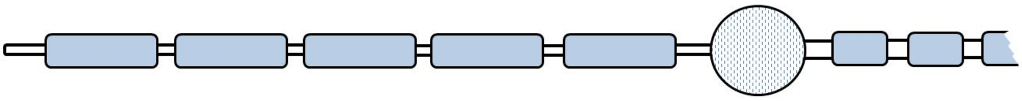

Figure 2.2 – Scheme of the human ANF morphology as used by Smit et al. (2010)

diameter of 3 µm except for the somatic region, which is 1 µm thinner. This reduction in diameter affects both the presomatic region and the adjacent nodes. The presomatic region and the soma are shielded by four layers of myelin. The model does not include a postsomatic region.

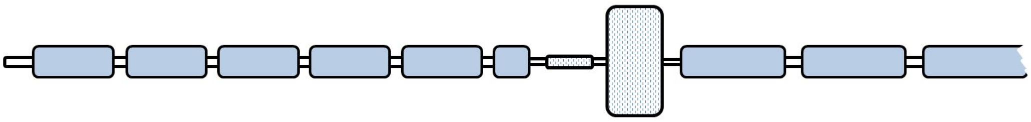

Figure 2.3 – Scheme of the human ANF morphology as used by Briaire and Frijns (2005)

Axon models

The axon models by Frijns et al. (1994), Smit et al. (2009) and Imennov and Rubinstein (2009) do not include morphologic components apart from nodes and internodes. The model of Frijns et al. (1994) has the largest dimensions with an outer diameter of 15 µm and 1.5 mm long internodes. The axon as modeled by Imennov and Rubinstein (2009) is distinctly smaller with an outer diameter of 2.5 µm. Additionally the nodes are constricted, which leads to a reduced nodal surface area by a factor of two. Smit et al. (2009) fitted their model to work for different outer fiber diameters between 5 µm and 15 µm. Thus the inner diameter, internodal lengths and the number of myelin layers are functions of the outer diameter.

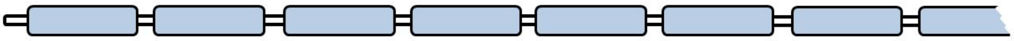

Figure 2.4 – Scheme of the morphology as used for the axon models

2.3 Electrical equivalent circuits

Each morphologic component of the ANF models is usually represented as one compartment. Nodes, the peripheral terminal, pre- and postsomatic regions and the soma are active compartments, which means that they have voltage-dependend ion channels and elicit action potentials. Internodes are passive compartments without ion channel activity. They can forward action potentials but not generate them.

Rattay et al. (2001)

For the electrical equivalent circuit of the active compartments, Rattay et al. (2001) followed the approach of Hodgkin and Huxley (1952). The cell membrane of the compartments is modeled as a capacitor, which can be charged or discharged by ionic currents. These currents depend on the membrane's ionic permeabilities, represented by voltage-dependend conductances, and the Nernst potentials of the ion species, modeled as batteries.

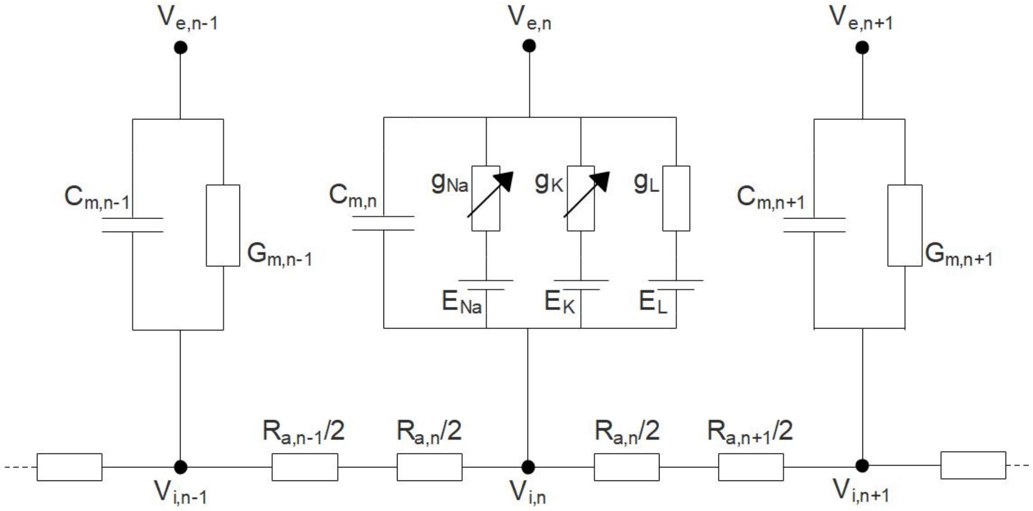

Figure 2.5 – Electrical equivalent circuit diagram of an active compartment in between two passive compartments. The electric components of the active compartment are: voltage-dependend membrane conductivities g_{Na} and g_{K} of the sodium and potassium channels; constant conductivity g_{L} for the leakage current; corresponding Nernst potentials E_{Na}, E_{K} and E_{L}; capacitance C_{m}; axoplasmatic resistance to the neighbors $R_{\mathrm{a}}/2$. The external and internal potentials at compartment n are given as $V_{\mathrm{e,n}}$ and $V_{\mathrm{i,n}}$, respectively. The passive compartments are described with the capacitance C_{m} and conductance G_{m}

.

The internodes are modeled as passive resistor-capacitor network. The capacitance C_{m} and conductance G_{m} of an internode with capacity c_{m}, conductivity g_{m}, membrane surface area A_{m} and N myelin layers is calculated following:

$$C_m = A_m \frac{c_m}{1+N}, \tag{2.1}$$

$$G_m = A_m \frac{g_m}{1+N}. \tag{2.2}$$

From these equation follows, that a bigger number of myelin layers goes along with both a lower capacitance and a lower conductance of the internodal membrane. So the current loss while passing the internodes can be minimized with a high degree of myelination. The electric equivalent circuit diagram for active and passive compartments in the model by Rattay et al. (2001) is depicted in Fig. 2.5.

The membrane voltage V_n is defined as the difference between the internal potential $V_\text{i,n}$ and the external potential $V_\text{e,n}$ at compartment n. The ionic currents can be summed up to I_ion. Using this nomenclature and applying Kirchhoff's current law to the equivalent circuit as shown in Fig. 2.5 results in the following differential equation for V_n (Rattay et al., 2001):

$$\begin{aligned}\frac{dV_\text{n}}{dt} = \Big[-I_\text{ion} + \frac{V_\text{n-1} - V_\text{n}}{R_\text{a,n-1}/2 + R_\text{a,n}/2} + \frac{V_\text{n+1} - V_\text{n}}{R_\text{a,n+1}/2 + R_\text{a,n}/2} + \\ \frac{V_\text{e,n-1} - V_\text{e,n}}{R_\text{a,n-1}/2 + R_\text{a,n}/2} + \frac{V_\text{e,n+1} - V_\text{e,n}}{R_\text{a,n+1}/2 + R_\text{a,n}/2} \Big] / C_\text{m,n},\end{aligned} \tag{2.3}$$

in which the two terms including V_e are called activating function, as they describe, how the ANF is activated due to external stimulation.

Smit et al. (2009)

Smit et al. (2009) also followed the approach of the HH model for active compartments. For the passive internodes, however, they used a double cable structure as proposed by Blight (1985). Hence a distinction was made between the isolating properties of the axolemma and the myelin sheath. Figure 2.6 depicts the electrical equivalent circuit diagram of an internode.

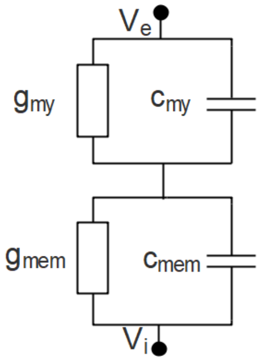

Figure 2.6 – Double cable structure of an internode as used by Smit et al. (2009). The myelin layers are characterized by the conductivity g_my and the capacity c_my. The corresponding parameters for the axolemma are g_mem and c_mem.

Both the conductivity g_mem and the capacity c_men of the axolemma are distinctly higher than the values of the myelin layers (g_my and c_my). The conductance

G_{m} and capacitance C_{m} of the entire cell isolation, consisting of the axolemma and N myelin layers, can be calculated following:

$$G_{\mathrm{m}} = A_{\mathrm{m}} \frac{1}{\frac{1}{g_{\mathrm{mem}}} + \frac{N}{g_{\mathrm{my}}}}, \tag{2.4}$$

$$C_{\mathrm{m}} = A_{\mathrm{m}} \frac{1}{\frac{1}{c_{\mathrm{mem}}} + \frac{N}{c_{\mathrm{my}}}}, \tag{2.5}$$

where A_{m} denotes the internodal surface area.

Smit et al. (2010)

Smit et al. (2010) combined the approaches of Rattay et al. (2001) and Smit et al. (2009) in their human ANF model. Therefore the electrical equivalent circuits of the dendrite are the same as in the model by Rattay et al. (2001) and for the axon they follow the approach of Smit et al. (2009).

Frijns et al. (1994) and Briaire and Frijns (2005)

The active compartments in the ANF models by Frijns et al. (1994) and Briaire and Frijns (2005) were constructed as proposed by Frankenhaeuser and Huxley (1964). Therefore the ion channels are represented by voltage dependent ionic permeabilities in place of conductances as used in the HH model. How this affects the calculation of the ion currents is part of Sec. 2.4.

The myelin sheath was treated as a perfect insulator, so both internodal capacity and conductivity were assumed to be zero. Thus the impact of the internodes and their morphologies is confined to their axoplasmatic resistances.

Imennov and Rubinstein (2009) and Negm and Bruce (2014)

Imennov and Rubinstein (2009) and Negm and Bruce (2014) published stochastic models, using a channel-number-tracking (CNT) algorithm (detailed in Sec. 2.6). The use of CNT results in a modification of the equivalent circuit for active compartments. Every single channel is modeled as a combination of a conductance γ and a switch. Closed switches represent open and activated channels. To obtain the total conductivity of a certain ion, the single-channel-conductivities of all conducting channels have to be summed up. Figure 2.7 depicts the described equivalent circuit diagram of an active compartment with sodium and potassium channels.

The internodes in the axon model of Imennov and Rubinstein (2009) were divided into nine equally spaced segments. Each segment was modeled as one

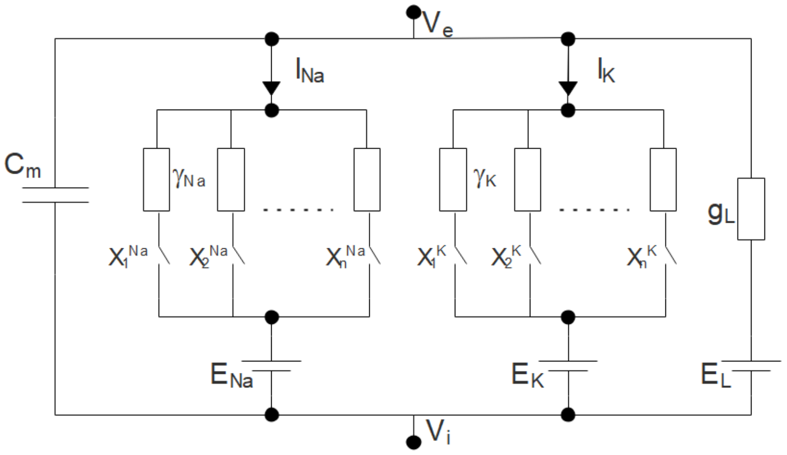

Figure 2.7 – Electrical equivalent circuit diagram of an active compartment as used in the stochastic models by Imennov and Rubinstein (2009) and Negm and Bruce (2014). γ_{Na} and γ_{K} are the single-channel conductances of sodium and potassium, which are depicted representatively for other ion species used in the models. $X_{\mathrm{i}}^{\mathrm{Na}}$ and $X_{\mathrm{i}}^{\mathrm{K}}$ are the corresponding stochastic single-channel states, which can be open or closed. The rest of the parameters was explained in Fig. 2.5.

compartment with a passive resistor-capacitor network. The purpose of splitting internodes in more than one compartment is to approximate the solution of the continuous cable equation more closely.

2.4 Ion currents, channel types and gating properties

The differential equation 2.3, explained in the previous section, describes the time course of the membrane voltage in every compartment. It contains the term I_{ion}, which is the sum of all ionic currents in a model. This section explains the methods used to calculate the ionic currents, the variety of used channel types and the corresponding gating properties.

Rattay et al. (2001)

Rattay et al. (2001) adopted the channel types and gating properties from the original HH model. Hence their model includes sodium and potassium channels, represented in the electrical equivalent circuit by the conductances g_{Na} and g_{K} and the respective Nernst potentials E_{Na} and E_{K} (see Fig. 2.5). The sodium current i_{Na} and the potassium current i_{K} are calculated following

$$i_{\mathrm{Na}} = \overline{g}_{\mathrm{Na}} m^3 h (V - E_{\mathrm{Na}}), \tag{2.6}$$

$$i_{\mathrm{K}} = \overline{g}_{\mathrm{K}} n^4 (V - E_{\mathrm{K}}), \tag{2.7}$$

where $\overline{g}_{\mathrm{Na}}$ and $\overline{g}_{\mathrm{K}}$ denote the maximum conductivities of the sodium and potassium channels, respectively. They are multiplied with gating variables which describe the opening probabilities and can take values between zero and one. The gating variable used for potassium channels is n. The channels have to perform four transitions to be open, so n is taken to the power of four. Sodium channels need three transitions. Additionally to the opening probability, described by m, the sodium channels have to perform an activation process. The probability for the channels to be activated is represented by the gating variable h. The maximum conductivities are reached when all channels are open (and activated in case of sodium). In general a gating variable x is described with the following differential equation:

$$\frac{dx}{dt} = \alpha_{\mathrm{x}}(1 - x) - \beta_{\mathrm{x}} x, \tag{2.8}$$

where α_{x} and β_{x} denote opening and closing rates, respectively. They are voltage dependent and define the steady-state value and time constant of a gating variable x. The equations for α_{x} and β_{x} are called rate equations and can be looked up in Hodgkin and Huxley (1952).

Rattay et al. (2001) adopted all parameters from the HH model, but made two adjustments. Firstly, the channel conductances were multiplied by 10 in all active compartments except for the soma to simulate 10-fold channel density. Secondly, the right sides of the differential equations for the gating variables were multiplied by 12 to account for the faster gating processes in mammalian axons compared to the ones in the squid, measured by Hodgkin and Huxley (1952) at 6.3°C. Figure 2.8 shows the resulting gating properties for the sodium and potassium channels. In this and further figures the resting potential V_{res} has been shifted to 0 V for an easier comparison. Figure 2.8a depicts the steady-state values of the gating variables m, h and n at certain membrane voltages, which will be reached with the time constants τ_{m}, τ_{h} and τ_{n} as shown in Fig. 2.8b. The underlying mechanisms of action potential generation can be comprehended by inspecting these gating properties: Most of the potassium channels and nearly all sodium channels are closed at resting state. An increase of the membrane potential due to a sufficient stimulus, results in the opening of both potassium and sodium channels. As τ_{m} is distinctly smaller than τ_{n} (see 2.8b), an inflow of sodium will be the first consequence of the stimulus. The inflow increases the membrane potential further and even more sodium channels open. This self-accelerating process, called depolarization, is stopped as soon as the membrane potential almost reaches the Nernst potential of sodium (115 mV above V_{res}) since most of the sodium channels become inactivated and the potassium channels are finally opened (see gating variables h and n in 2.8). The following outflow of potassium repolarizes the cell towards the Nernst potential of potassium (-12 mV). After a short period of hyperpolarisation (membrane potential is below V_{res}), the cell returns to resting state again.

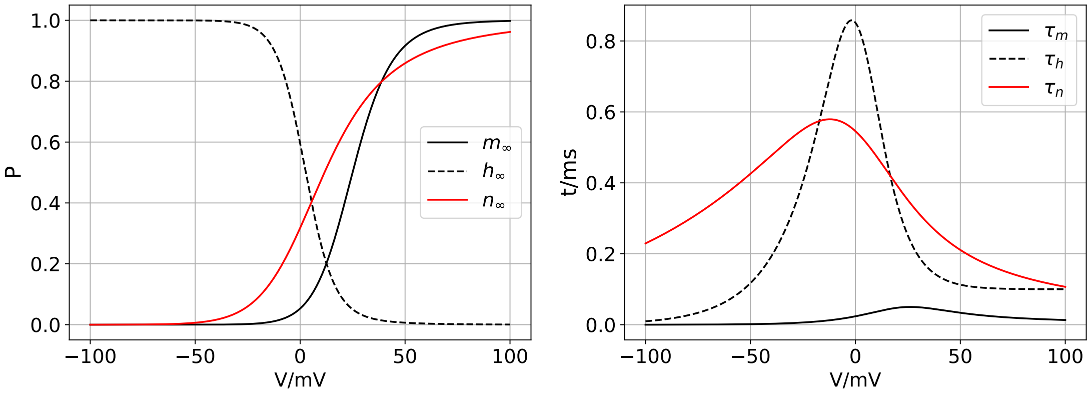

(a) Steady-state values

(b) Time constants

Figure 2.8 – Gating properties of the sodium and potassium channels in the model by Rattay et al. (2001).

Figure 2.8a shows that there is ion channel activity in resting state. Hence an unspecified leakage current is added to the ionic currents to ensure that the total transmembrane current is zero in resting state. Such a leakage current is used in all of the presented models.

Smit et al. (2009)

Like the model of Rattay et al. (2001), the model by Smit et al. (2009) is based on the original HH model, but the values for the channel conductances and Nernst potentials differ from the ones suggested by Hodgkin and Huxley. Furthermore the original rate equations were multiplied by individual factors. This changed the time constants of the gating variables, which can be seen in Fig. 2.9b, whereas the steady-state values remained the same as in the HH model. The most obvious difference is the slowdown of the opening process of the potassium channels. The existence of slow potassium channels was evidenced by several rat experiences (Safronov et al., 1993; Scholz et al., 1993; Reid et al., 1999; Roper and Schwarz, 2000). Although five different types of fast, intermediate and slow potassium channels have been recorded in human nerve fibers (Reid et al., 1999), Smit et al. (2009) solely included the slowest channel type in their model. This was justified by the fact, that most of the fast and intermediate potassium channels cluster underneath the myelin sheath (Smit et al., 2010), i.e. their realistic densities at nodes are lower than assumed by Hodgkin and Huxley and lower than the density of slow potassium channels (McIntyre et al., 2002). Another modification in the model by Smit et al. (2009), is the subdivision of the sodium current into two functionally distinct components. In addition to the transient one as introduced in the HH model, a persistent sodium current with gating variable m_{p} was used based on rat experiments (Caldwell et al., 2000; Honmou et al., 1994). The persistent sodium channels open at higher membrane potentials and they open slower than the transient ones, which both can be seen in Fig. 2.9. Their proportion among all sodium channels was chosen to be 2.5%.

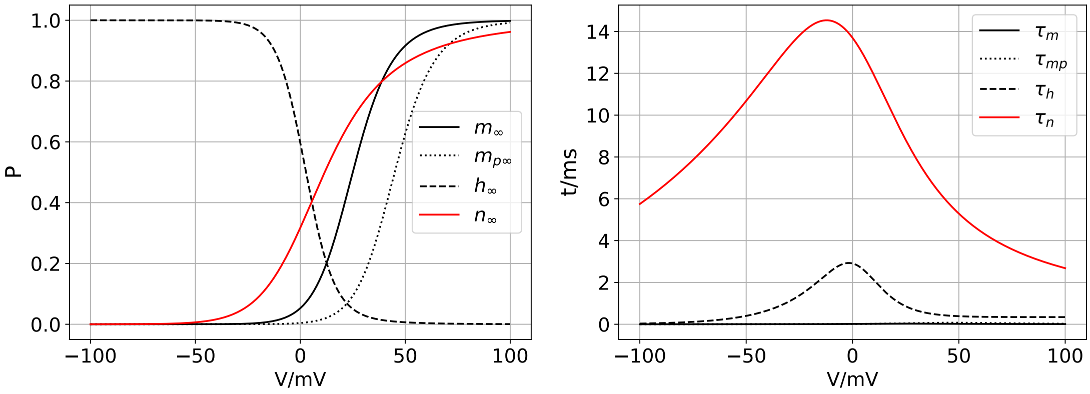

(a) Steady-state values

(b) Time constants

Figure 2.9 – Gating properties of the sodium and potassium channels in the model by Smit et al. (2009). The peaks of τ_{m} and τ_{mp} are not visible due to the scaling. The maximum value of τ_{m} is 0.03 ms and reached at 25 mV. τ_{mp} has a maximum of 0.075 ms for a membrane potential of 45 mV.

Smit et al. (2010)

For the dendrite and the soma of the human ANF model, Smit et al. (2010) used the same channel types and gating properties as Rattay et al. (2001) whereas the axon followed the approach of Smit et al. (2009).

Frijns et al. (1994) and Briaire and Frijns (2005)

Frijns et al. (1994) and Briaire and Frijns (2005) adapted an approach of Frankenhaeuser and Huxley (1964) and modeled the ion channels as voltage-dependent ionic permeabilities in place of membrane conductances as used in the HH model. This led to the following equations for the sodium and potassium channels:

$$i_{\mathrm{Na}} = \overline{P}_{\mathrm{Na}} h m^3 \cdot \frac{VF}{RT} \cdot \frac{[Na^+]_{\mathrm{e}} - [Na^+]_{\mathrm{i}} exp(\frac{VF}{RT})}{1 - exp(\frac{VF}{RT})}, \tag{2.9}$$

$$i_{\mathrm{K}} = \overline{P}_{\mathrm{K}} n^2 \cdot \frac{VF}{RT} \cdot \frac{[K^+]_{\mathrm{e}} - [K^+]_{\mathrm{i}} exp(\frac{VF}{RT})}{1 - exp(\frac{VF}{RT})}, \tag{2.10}$$

where $\overline{P}_{\mathrm{Na}}$ and $\overline{P}_{\mathrm{K}}$ are the respective maximum permeabilities of the sodium and potassium channels and multiplied with corresponding gating variables. Different to the HH model, the potassium channels perform only two transitions, so n is taken to the power of two. The Eq. 2.9 and 2.10 contain the intracellular concentrations $[Na^+]_{\mathrm{i}}$ and $[K^+]_{\mathrm{i}}$ and the extracellular concentrations $[Na^+]_{\mathrm{e}}$ and $[K^+]_{\mathrm{e}}$ of sodium and potassium, respectively. The rest of the parameters are the absolute temperature T, the Faraday constant F and the gas constant R. Apart from sodium and potassium no further channel types have been included.

Frijns et al. (1994) and Briaire and Frijns (2005) used the gating properties as proposed by Schwarz and Eikhof (1987) (SE), who published a model based on experiments with cats and rats. The differential equations of the gating variables in the SE model are the same as in the HH model (see Eq. 2.8), but there are differences in the calculation of the voltage dependent opening and closing rates. The resulting gating characteristics are depicted in Fig. 2.10. Both the steady-state values and the time constants of the gating variables in the SE model are similar to the ones in the warm HH model. The biggest differences can be observed for the opening process of the potassium channels. The steady-state curve of n is shifted towards higher potentials and is steeper than in the HH model so that the function almost equals the one of m. The maximum value of τ_{n} is higher in the SE model and is reached at about 30 mV in contrast to −20 mV in the HH model.

Imennov and Rubinstein (2009)

As mentioned in Sec. 2.3, Imennov and Rubinstein (2009) modeled the channel transitions as a stochastic process and used a channel number tracking algorithm (CNT). This altered the equations for the ion currents, which is shown in Eq. 2.11 on the example of sodium.

$$i_{\mathrm{Na}} = \gamma_{\mathrm{Na}} N_{m_3 h_1} (V - E_{Na}) \tag{2.11}$$

The single sodium channel conductance γ_{Na} is multiplied with $N_{m_3 h_1}$, which is the number of sodium channels in the conducting state. This is reached, when all

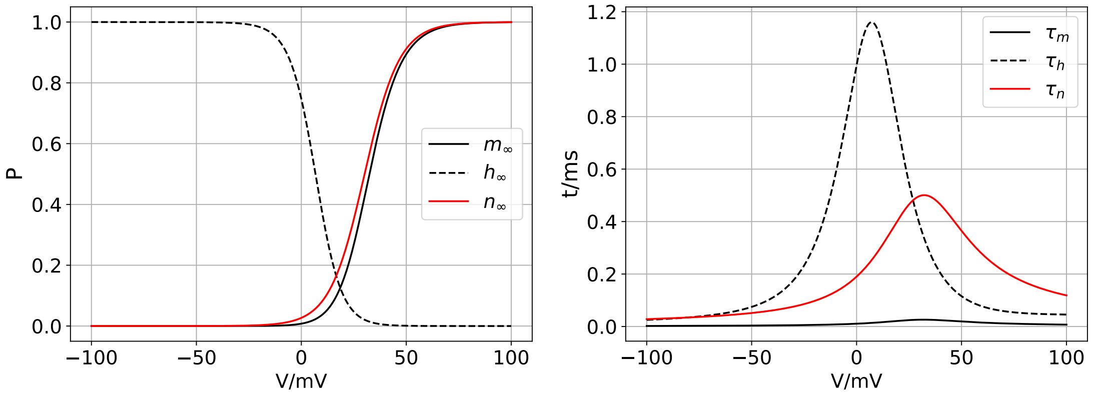

(a) Steady-state values

(b) Time constants

Figure 2.10 – Gating properties of the sodium and potassium channels as proposed by Schwarz and Eikhof (1987) and adopted by Frijns et al. (1994) and Briaire and Frijns (2005).

three transitions were done to open the channel and it is activated additionally. The CNT algorithm was used for all channel types in the model.

Imennov and Rubinstein (2009) used strongly modified versions of the rate equations of the SE model. Most of the changes were adopted from the model by McIntyre et al. (2002). The resulting channel characteristics are depicted in Fig. 2.11.

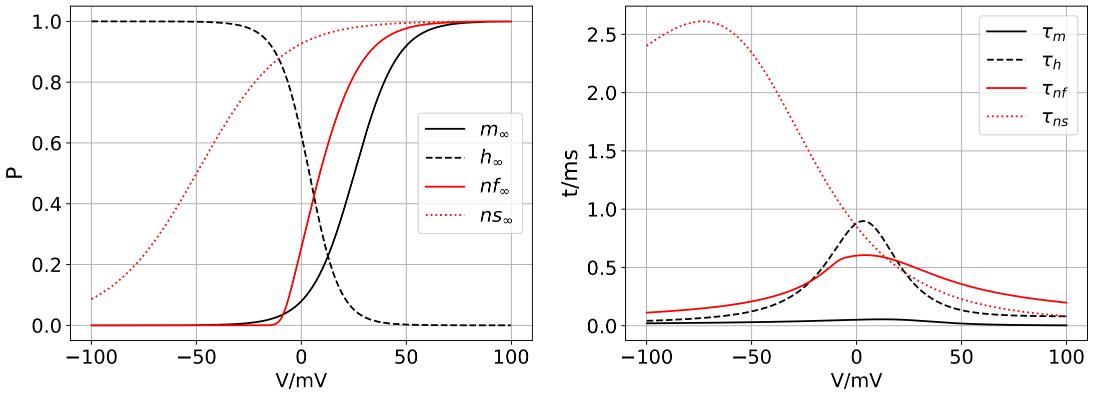

(a) Steady-state values

(b) Time constants

Figure 2.11 – Gating properties of the sodium and potassium channels in the model by Imennov and Rubinstein (2009).

The potassium current is modeled as two distinct components. As already mentioned Reid et al. (1999) recorded slow, intermediate and fast potassium channels in human nerve fibers. The first component I_{kf} with gating variable nf models the fast and intermediate potassium channels and the second component I_{ks} with gating variable ns represents the slow ones. These open at lower membrane potentials than the faster channels and have slow dynamics below V_{res}. The maximum channel density of the slow potassium channels was defined to be twice as big as the density of the faster type. The gating properties of the sodium channels are similar to the ones in the SE model.

Negm and Bruce (2014)

Negm and Bruce (2014) also used the CNT algorithm with stochastic channel transitions and applied it to all ion channel types. Like Imennov and Rubinstein (2009), they used modified versions of the rate equations as published by Schwarz and Eikhof (1987). This leads to the gating characteristics of sodium and potassium as shown in Fig. 2.12. The opening and activation process of the sodium channels remained the same as in the SE model, but differences can be observed for the opening probability of potassium. The steady-state curve rises less steep than in the SE model and the maximum of τ_n is reached for the same potential, but is about two times lower.

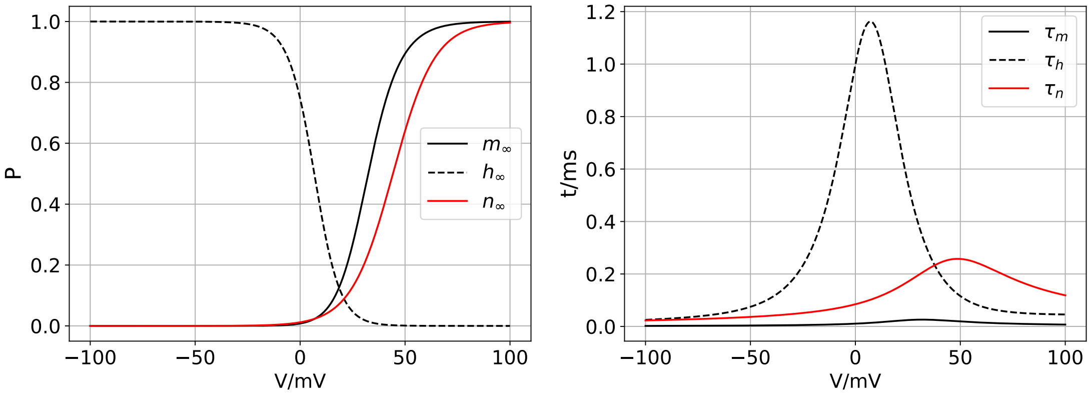

(a) Steady-state values **(b)** Time constants

Figure 2.12 – Gating properties of the sodium and potassium channels in the single node model by Negm and Bruce (2014).

Negm and Bruce (2014) added two further voltage dependent channel types to their model aiming the inclusion of adaptation, firstly hyperpolarization-activated cation (HCN) channels and secondly low-threshold potassium (KLT) channels. The HCN and KLT channels permit the passage of the currents I_{h} and I_{KLT}. I_{h} is characterized to be a mixed cation current, since the HCN channels are permeable to both sodium and potassium ions. They have been found and investigated with voltage clamp measurements in i.a. the spiral ganglion neurons of mouses (Mo and Davis, 1997), guinea pigs (Chen, 1997) and rats (Yi et al., 2010). The KLT channels were i.a. evidenced by experiments on murine spiral ganglion neurons (Adamson et al., 2002; Mo et al., 2002), where their contribution to adaptation has been shown. A detailed description regarding how adaptation is modeled using HCN and KLT channels is given in the following section.

2.5 Adaptation and accommodation

Adaptation and accommodation are temporal characteristics that have been observed in ANFs in several experiments (Javel and Shepherd, 2001; Zhang et al., 2007; Miller et al., 2008). Accommodation describes a threshold increase caused by long-term stimulation or high-rate pulse trains. Adaptation refers to a threshold increase in consequence of ongoing spiking. Classic single node models as the one by Hodgkin and Huxley (1952) and most of the contemporary biophysical ANF models can not account for the effects of adaptation and accommodation. These long-term mechanisms, however, are likely to have an important impact on the perception of CI users (Schmidt Clay and Brown, 2007). Consequently, approaches for adaptive biophysical ANF models have been published. As adaptation and accommodation are related and it is often difficult to keep them apart, the term adaptation will be used for both effects in the following.

Woo et al. (2009) modeled adaptation using a dynamic external potassium concentration $[K^+]_e$ and applied it to a feline ANF model (Woo et al., 2010). The idea is based on the findings by Baylor and Nicholls (1969), who showed in experiments on the leech, that $[K^+]_e$ changes can cause adaptation-like effects. Even though, there is no experimental evidence that an ongoing stimulation of a nerve fiber can alter $[K^+]_e$ distinctly. For this reason the approach by Woo et al. (2009) was not implemented in this work.

Negm and Bruce (2014) incorporated adaptation by adding two voltage dependent ion channel types to their single node model which have already been introduced in Sec. 2.4. The HCN channels have an opening process, described with gating variable r and the Nernst potential is 35 mV above V_{res}. The KLT channels have an opening process, described with gating variable w and an inactivation process with gating variable z. The corresponding gating properties are depicted in Fig. 2.13. Due to their respective Nernst potentials, the membrane is constantly charged by I_{h} and discharged by I_{KLT} even in resting state. Figure 2.13a shows, that membrane voltages above V_{res} lower the opening probability of the HCN channels and increase it for the KLT channels. Thus APs lead to a decrease of I_{h} and an increase of I_{KLT} and therefore to a lower membrane equilibrium potential and a diminished excitability. This results in adaptation-like effects for ongoing pulse trains, whereby the HCN channels have the slower effect, which can be explained with the time constants of the gating variables as depicted in Fig. 2.13b.

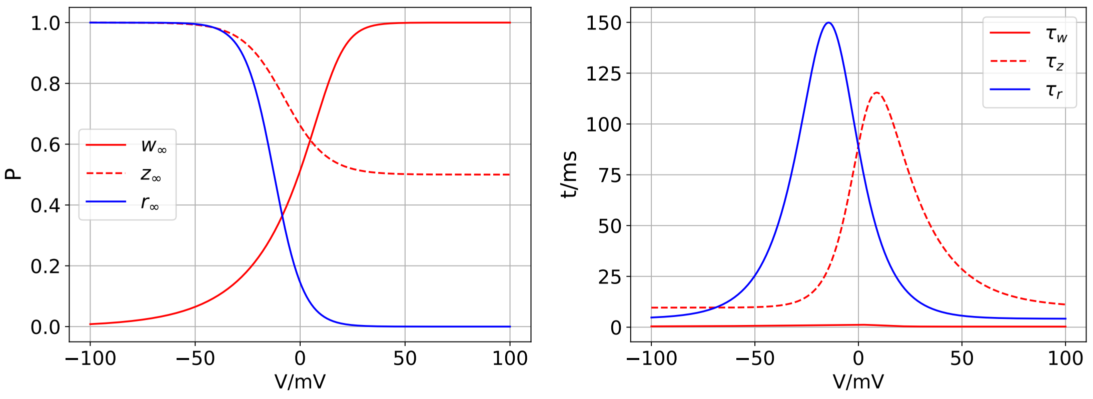

(a) Steady-state values **(b)** Time constants

Figure 2.13 – Gating properties of the KLT and HCN channels in the model by Negm and Bruce (2014).

2.6 Inclusion of stochasticity

The classic biophysical single node models such as the HH and SE model are deterministic, which means that the same stimulus always provides exactly the same spiking behaviour. This is sufficient for the prediction of a number of nerve fiber properties such as the threshold, refractory periods and conduction velocity. Real ANFs, however, are not deterministic, which was shown by Verveen (1960) who described spike timing and threshold fluctuations. These can be explained by channel noise, which represents the seemingly random transitions of individual ion channels between open and closed states (O'Brien and Rubinstein, 2016). In order to describe probabilistic response properties as the relative spread of thresholds and jitter, the stochastic nature of the ion channels has to be represented in an ANF model (Imennov and Rubinstein, 2009). Among the models implemented in this thesis, only the ones by Rattay et al. (2001), Imennov and Rubinstein (2009) and Negm and Bruce (2014) included stochasticity. The other models were deterministic. This section gives an overview about different methods to account for channel noise and compares them with regard to their exactness and computational efficiency.

Gaussian noise current term

A simple approach to include stochasticity was used by Rattay et al. (2001) who adopted an approach of Rubinstein (1995). The channel noise is modeled by a Gaussian noise current term i_{noise}, which is added to the total ion current i_{ion} (see Eq. 2.3) and calculated with:

$$i_{noise} = X \cdot k_{\mathrm{noise}} \sqrt{A g_{\mathrm{Na}}}, \tag{2.12}$$

where X is a Gaussian random variable, which continually changes its value with every time step. This is multiplied with the factor k_{noise}, which is common for all compartments and used to adjust how strong the stochastic behavior of the channels is emphasized. The noise current term also depends on the maximum sodium conductivity g_{Na} and the membrane surface area A. This approach is easy to implement and the computational costs are very small. It is inexact however, as it does not include a dependency on the membrane voltage and it was shown that membrane noise increases for higher deviations from V_{res} (Verveen and Derksen, 1968).

Markov jumping process and channel number tracking algorithm

The single node model by Negm and Bruce (2014) and the axon model by Imennov and Rubinstein (2009) produced stochastic responses using a channel number tracking (CNT) algorithm with channel transitions follwing a Markov jumping process. This approach was developed by Gillespie (1977) and initially used for modeling stochastic membrane mechanisms in neurons by Chow and White (1996). The idea behind the CNT algorithm is briefly described in the following. A detailed description can be found in the appendix of the paper by Mino et al. (2002).

As already mentioned, the channels have to perform a few transformations to be open. The CNT algorithm tracks the number of channels in each of the possible conformations, i.e. ”states”. After a certain time-step, one of the channels changes its state. Both the length of the time-step and the kind of transformation depend on a Gaussian random variable and the opening and closing rates. As the rate equations are voltage dependent, the experimentally shown dependency of channel noise on the membrane voltage (Verveen and Derksen, 1968) applies in this approach. Consequently, algorithms using Markov processes were found to be the most accurate ones to model channel noise. Among them the CNT algorithm turned out to be the most efficient one (Mino et al., 2002).

Chapter 3

Implementation

The ANF models, described in the previous chapter and listed in Table 2.1 have been implemented for this thesis. The implementation was done in Python 3.4, using the Brian2 package (Goodman and Brette, 2009). Brian is a simulator for spiking neural networks and provides for an efficient numerical solution of differential equations. The exponential Euler was the chosen integration method for all models.

The ambition of the implementation was to be as close as possible to the original ANF model versions using all parameters and methods as published. In some cases, however, this was not feasible because of missing or ambiguous information or out of computational reasons. Such cases are listed as follows:

Rattay et al. (2001) did not provide values for the lengths of the dendritic internodes in their model. In this work 350 µm have been used as the resulting action potential (AP) propagation pattern compared well with the one depicted in their paper. The dendritic internodes in the model of Briaire and Frijns (2005) were described as scalable in order to adjust for the variable length from the organ of Corti to the soma. Their length was set to 175 µm here as this value was used in a previous model version (Frijns et al., 2000). The illustration of the ANF morphology in the paper of Briaire and Frijns (2005) also indicated short dendritic internodes.

As mentioned, Smit et al. (2009) published an axon model which was fitted for fiber diameters ranging from 5 µm to 15 µm. The model parameters had initially been developed and optimized for a 15 µm diameter, though, and were then scaled down to model thinner fibers. Thus for the purpose of this study only the thickest ANF version was implemented and investigated.

The values for the capacitance of both nodes and internodes in the model of Imennov and Rubinstein (2009) were presumably published with the wrong entity. A comparison with the referenced paper (Tasaki, 1955) suggested the use of distinctly higher capacitances.

The compartments of all ANF models were implemented as cylinders or frustums in Brian2. To approximate the spherical shape of the soma in the models of Rattay et al. (2001) and Smit et al. (2010), it had to be segmented into multiple compartments. A number of 10 segments proved to be sufficient as further compartments did not alter the model proporties considerably. Furthermore, the internodes in the axon model of Imennov and Rubinstein (2009) were segmented into nine equally spaced parts and three compartments were used for the presomatic regions in the human ANF models. This was both done in accordance with the information given in the respective papers. All other morpholigic components were modeled as one compartment.

The node model of Negm and Bruce (2014) was extended to an ANF model using the morphology, axoplasmatic resistivity and insulating properties of the dendrite as modeled by Rattay et al. (2001). The extension was necessary in order to apply the same tests as to the other models and to obtain comparable results. In these tests, the membrane potential is usually measured at fiber positions different from the stimulus location. Otherwise an increase of the membrane potential caused by the stimulus current could easily be misinterpreted as an AP. This is unavoidable in node models which was another reason for the extension.

The CNT algorithm used by Imennov and Rubinstein (2009) and Negm and Bruce (2014) to simulate the stochastic processes of the ion channels was not implemented in this thesis. One reason was that Brian2 is not an appropriate tool to include Markov processes and it was desirable to have a consistent framework for all ANF models. Moreover it could not be assured that the CNT algorithm is efficient enough to compute responses for a population of nerve fibers in an acceptable period of time. Therefore deterministic versions of the models by Imennov and Rubinstein (2009) and Negm and Bruce (2014) were implemented. This was accomplished by replacing the stochastic description of the state transitions with the differential equations for the gating variables as used in the HH model (see Eq. 2.8).

A battery of various tests has been implemented to investigate the characteristics of the seven ANF models. The thorns package provided a multiprocessing tool which was used for most of the tests. The standard time step in simulations was chosen to be 5 µs. For some of the tests which required an increased temporal accuracy, a time step of 1 µs was used.

Chapter 4

Comparison of model characteristics

This chapter describes and compares a number of ANF characteristics measured with the models implemented in the thesis. Section 4.1 regards properties of single ANFs and compares them to experimental data. In Sec. 4.2 the spiking behavior of a population of 400 fibers is investigated for some of the models.

4.1 Single Fiber characteristics

The single fiber characteristics investigated in this section include the conduction velocity, thresholds, AP shape and latency, stochastic properties as well as refractory and adaptation behavior. The measurement procedures are explained in this section and the results of all models are compared with each other and to experimentally obtained data.

In all tests, the models were stimulated externally using a point electrode. Unless otherwise stated, the electrode was arranged above the third peripheral node with a distance of 500 µm to the fiber. The ANF responses were usually measured at the tenth node, which is at the axonal part of the models with a soma. The extracellular space was modeled as a homogeneous medium with a resistivity of $3\,\Omega\,\mathrm{m}$ except for the model of Imennov and Rubinstein (2009) who suggested an isotropic resistivity of $25\,\Omega\,\mathrm{m}$.

4.1.1 Thresholds

The threshold of an ANF model is referred to the minimum required current amplitude to elicit an AP. This section measures the impact of the phase length and polarity of a stimulus on the threshold of the models. Furthermore it is investigated how the thresholds are affected by the pulse rate and duration of pulse-trains. The threshold current for a certain stimulation pattern is in the following denoted as I_{th}.

Strength-duration characteristics

The relation between I_{th} and the duration of the applied stimulus is known as strength-duration curve. Figure 4.1 compares the strength-duration curves measured with the ANF models for both monophasic cathodic and anodic stimuli. It is a common situation for all models that the thresholds decreased with longer phase durations. The curves however converged to distinct minimum current amplitudes and phase durations. Short cathodic pulses of 1 µs and 2 µs, respectively, elicited APs with the models of Imennov and Rubinstein (2009) and Frijns et al. (1994). The other models required longer stimuli to charge the membrane sufficiently. The thresholds were higher for anodic pulses, but the difference to the cathodic stimulation varied among models.

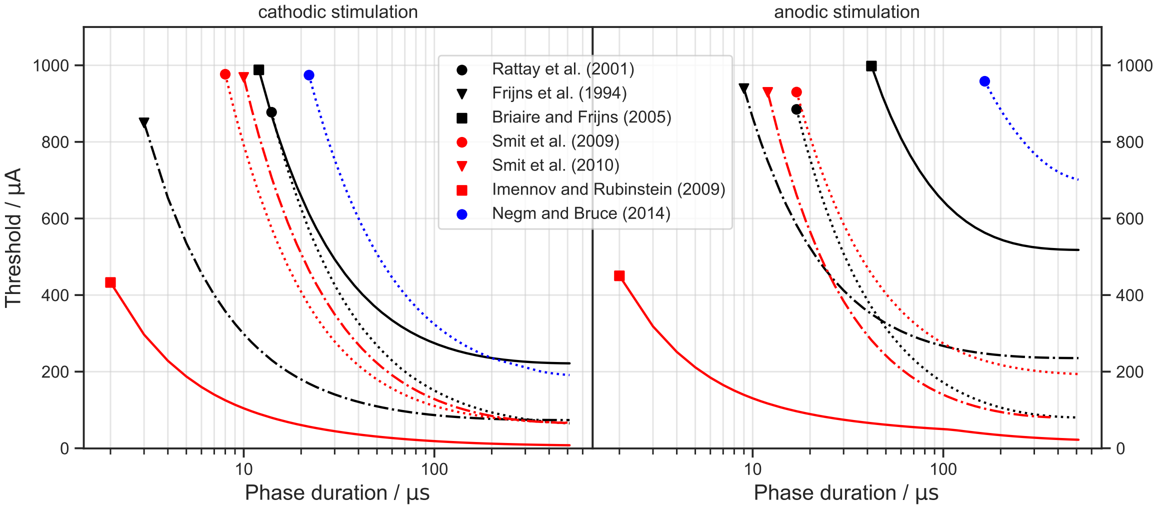

Figure 4.1 – Comparison of strength-duration curves for monophasic cathodic (left) and anodic (right) stimuli. The abscissa is in log-scale for a better discriminability of the curves.

The current threshold to which the strength-duration curves converge for very long pulses is called rheobase I_{rh}. The chronaxie τ_{chr} defines the required pulse length to elicit an AP when applying twice I_{rh}. These two values are used to characterize the strength-duration behavior of a nerve fiber. Table 4.1 compares the values for I_{rh} and τ_{chr} measured with the ANF models.

Table 4.1 – Comparison of rheobase I_{rh} and chronaxie τ_{chr} of the ANF models for monophasic cathodic and anodic stimulation.

	cathodic		anodic	
	$I_{\mathrm{rh}}/\mu\mathrm{A}$	$\tau_{\mathrm{chr}}/\mu\mathrm{s}$	$I_{\mathrm{rh}}/\mu\mathrm{A}$	$\tau_{\mathrm{chr}}/\mu\mathrm{s}$
Rattay et al. (2001)	63.2	128	79.8	110
Frijns et al. (1994)	73.5	28.3	235	24.4
Briaire and Frijns (2005)	221	36.1	518	40
Smit et al. (2009)	66.1	76.2	192	55.7
Smit et al. (2010)	64.7	93.8	79	85.9
Imennov and Rubinstein (2009)	6.6	170	18.7	173
Negm and Bruce (2014)	188	78.1	694	86.9

The values for I_{rh}, using cathodic stimuli, ranged from 10 µA (Imennov and Rubinstein, 2009) to 188 µA (Negm and Bruce, 2014) and were smaller than those, measured for anodic pulses. While the values of the models by Rattay et al. (2001) and Smit et al. (2010) differed only slightly among polarities, I_{rh} for anodic stimulation was increased by at least a factor of two in other models. The impact of the polarity on τ_{chr} was smaller and no clear tendency was discernible. The values ranged from 24.4 µs (Frijns et al., 1994) to 173 µs (Imennov and Rubinstein, 2009), both measured for anodic stimuli.

Smit et al. (2009) and Smit et al. (2010) included persistent sodium channels in their models to obtain a longer chronaxie. Tests showed, however, that τ_{chr} was only increased by 1 µs for cathodic pulses in both models. Applying anodic pulses, τ_{chr} was raised by 2 µs and 7 µs, respectively, after the inclusion of the persistent sodium channels.

Ranck (1975) described in a review that τ_{chr} between 29 µs and 100 µs were observed in mammalian nerve fibers. Van den Honert and Stypulkowski (1984) suggested a distinctly longer mean chronaxie of 264 µs obtained in feline experiments. Part of the variation in experimental data can be explained by differences in the method of stimulation and the distance between electrode and nerve fiber (Frijns et al., 1994). Ranck (1975) mentioned that τ_{chr} was often about 0.7 the time constant of the membrane, which is defined as the product of the membrane resistance and capacitance. This was independent of the stimulus polarity. The values for τ_{chr} measured with the ANF models are within the experimental range, despite that their relations to the membrane time constants could not be confirmed.

All models predicted higher thresholds for anodic stimulation. This was also shown in studies on feline nerve fibers. BeMent and Ranck (1969) found that anodic pulses required 3.19-7.7 times the current of cathodic pulses to excite the fiber. Armstrong et al. (1973) measured ratios of 1.0-3.2. The reason why a monophasic cathodic stimulus is more effective than an anodic one is illustrated in Fig. 4.2. Assuming a constant axoplasmatic resistance along a straight fiber, the activating function is proportional to the second derivative of the external membrane potential (see Eq. 2.3). In areas where the activating function is positive a fiber is depolarized whereas negative values lead to hyperpolarization. Figure 4.2 depicts that the positive peak for cathodic stimulation is higher than the two positive peaks obtained with anodic stimulation, which explains the different thresholds.

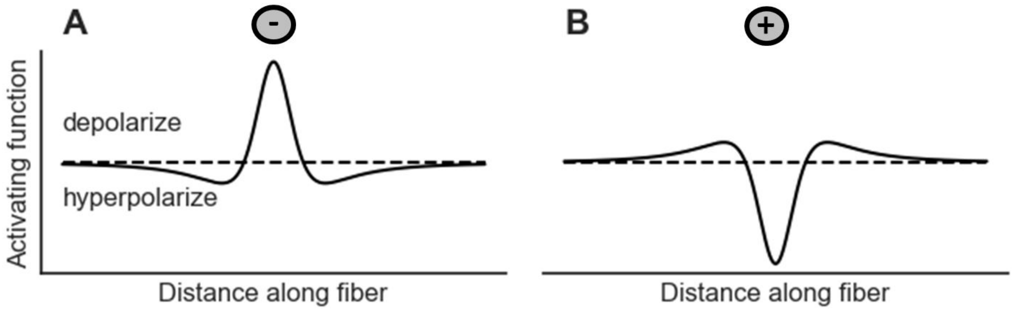

Figure 4.2 – Activating function along an axon for A: cathodic and B: anodic stimulation. The simplified case of a constant axoplasmatic resistance and a straight fiber was assumed.

Stimulating the ANF models with cathodic current pulses distinctly higher than I_{th} led to an unexpected behavior. The AP elicited in the depolarized area near the electrode could not propagate along the fiber. The hyperpolarized fiber regions with the negative activating function as shown in Fig. 4.2 turned out to be an insurmountable potential barrier and erased the AP.

Thresholds of pulse-trains

In order to investigate the role of integration, pulse-trains of biphasic (cathodic-first) pulses with 45 µs/phase and an 8 µs inter-phase gap were applied to the ANF models. Thresholds were measured as a function of pulse rate and train duration as depicted in Fig. 4.3.

The thresholds remained constant for pulse rates up to 2000 pulses per second (pps) and train durations longer than 1 ms. Most ANF models predicted decreasing thresholds for pulse rates higher than 1000 pps. The biggest reduction (up to 3 dB regarding the single pulse threshold) was measured with the model of Imennov and Rubinstein (2009). The model by Smit et al. (2010) showed a contrary effect: the pulse-train thresholds for 10000 pps were increased by more than 1 dB for all train durations longer than 0.3 ms. Hardly any differences to the single

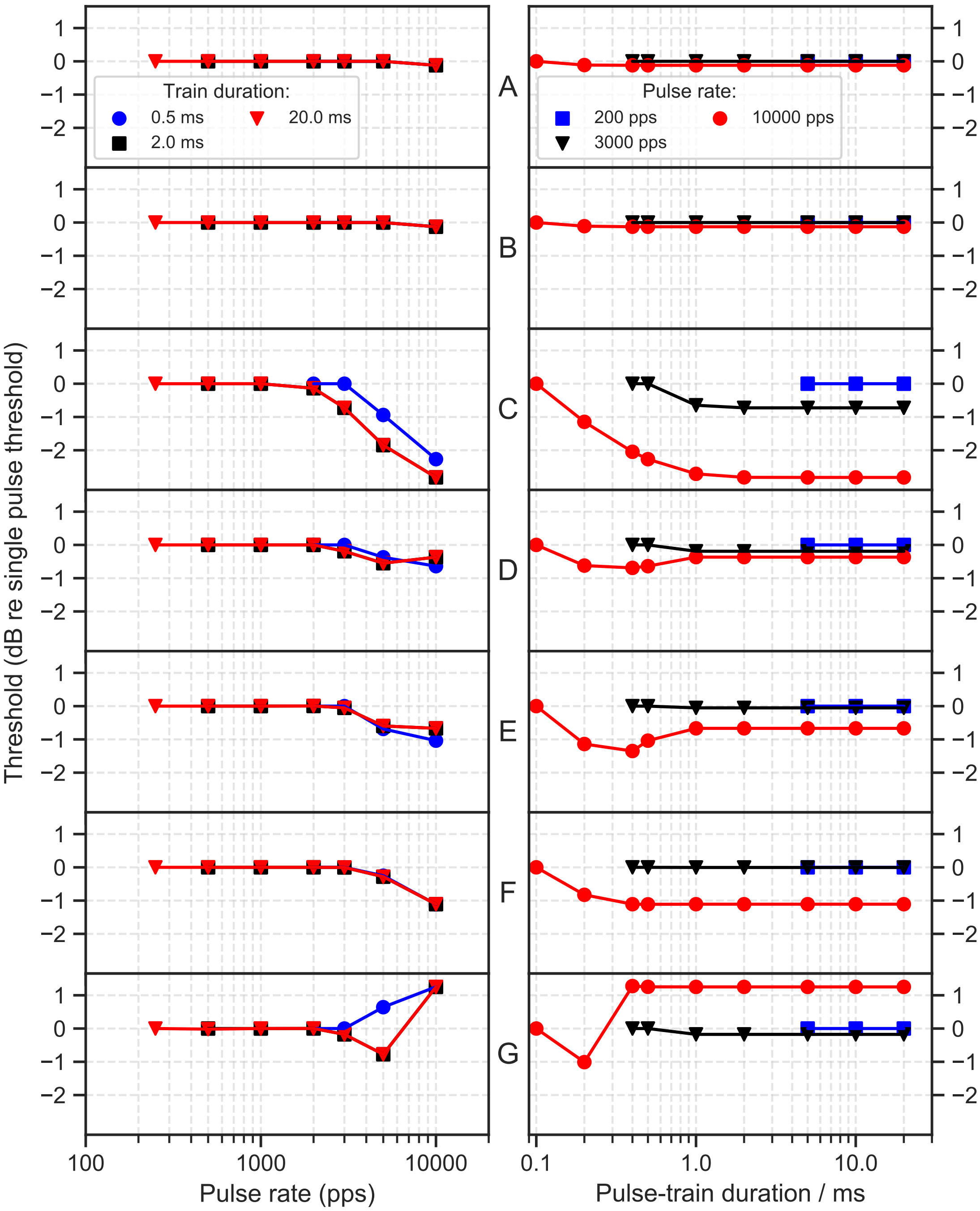

Figure 4.3 – Thresholds as a function of pulse rate (left column) and pulse-train duration (right column). **A**: Briaire and Frijns (2005); **B**: Frijns et al. (1994); **C**: Imennov and Rubinstein (2009); **D**: Negm and Bruce (2014); **E**: Rattay et al. (2001); **F**: Smit et al. (2009); **G**: Smit et al. (2010). Biphasic cathodic first 45 µs pulses with an inter-phase gap of 8 µs were used.

pulse threshold were obtained with the models by Briaire and Frijns (2005) and Frijns et al. (1994).

Zhou et al. (2015) measured the integration of pulse-trains in humans and guinea pigs with CIs and observed long-term integration up to 640 ms. This suggests a considerably longer temporal window over which pulses are integrated as predicted with the ANF models. Experiments with CI listeners have also shown that thresholds decrease with pulse rate. Carlyon et al. (2015) measured a drop of 3.9 dB from 71 pps to 500 pps and a larger drop of 7.7 dB from 500 pps to 3500 pps. Integration was observed for pulse rates even smaller than 10 pps (Zhou et al., 2015). These results lead to the conclusion that none of the models was able to predict pulse-train integration in a comparable range with the experimental results.

4.1.2 Conduction velocity

The conduction velocity v_c describes how fast an AP propagates along the nerve fiber. Seperate measurements of the dendritic and axonal velocities were performed in the human ANF models. Figure 4.4 depicts the measurement scheme for the dendrite. The electrode, which was placed above the second node, stimulated the ANF with a monophasic 100 µs cathodic pulse and amplitude $2I_\mathrm{th}$ and elicited an AP. Following this, the time period Δt between the APs at the second and second to last dendritic node were measured as well as their spatial distance Δs to calculate v_c as shown in Fig. 4.4. The same stimulus was used to measure the axonal conduction velocities of all models. Therefor the spike times were determined at the third and ante-penultimate axonal node.

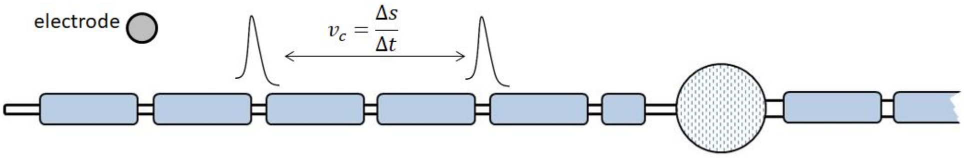

Figure 4.4 – Measurement scheme for dendritic conduction velocities.

Hursh (1939) found in experiments on feline nerve fibers that v_c increases linearly with the fibers' outer diameter D. He determined a scaling factor k of 6 which describes the ratio of v_c and D follwing:

$$k = \frac{v_\mathrm{c}/(\mathrm{ms}^{-1})}{D/\mathrm{\mu m}}. \tag{4.1}$$

Boyd and Kalu (1979) obtained two different scaling factors for distinct nerve fiber groups in measurements on cats. For thinner fiber groups with an outer diameter between 3 µm and 12 µm, they found a scaling factor of 4.6. The appropriate value for a thicker fiber group with an outer diameter between 10 µm and 21 µm turned out to be 5.7.

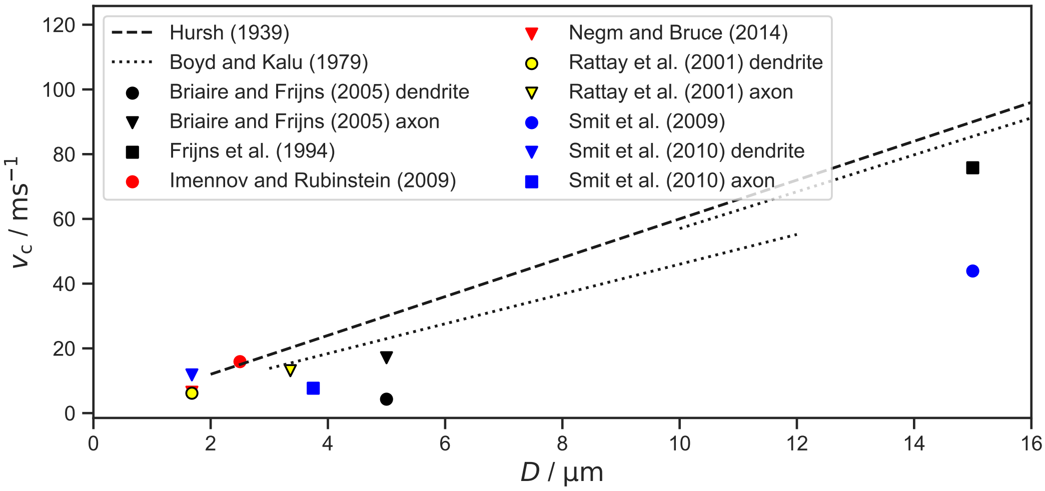

Figure 4.5 – Comparison of conduction velocities v_c, measured with the ANF models to experimental data. The velocities are plotted against the models respective outer diameters D.

Figure 4.5 compares the conduction velocities of the ANF models with the experimental results. For the majority of the models, both the outer diameters and the predicted conduction velocities were at the lower range of the values measured in the experiments. Exceptions are the axon models by Frijns et al. (1994) and Smit et al. (2009) which are distinctly thicker and predicted higher conduction velocities, accordingly. The exact values for the outer diameters of the models and the measured conduction velocities and scaling factors are listed in Tbl. 4.2. The scaling factors for the dendrite of the model by Briaire and Frijns (2005) and the axons as modeled by Smit et al. (2009) and Smit et al. (2010) are considerably smaller than the experimentally obtained values. The scaling factors of all other models are within 20% of the experimental results.

Czéh et al. (1976) found in feline experiments that the dendritic conduction velocity is usually higher than the axonal one and described the following relationship:

$$v_{\text{axon}} = 0.9 v_{\text{dendrite}} - 6.9 \frac{m}{s}. \tag{4.2}$$

Among the human ANF models, implemented in this thesis, only the one by Smit et al. (2010) predicted a faster conduction in the dendritic part. However, the difference to the axonal velocity was smaller than suggested by Czéh et al. (1976).

Table 4.2 – Comparison of conduction velocities, outer diameters and scaling factors predicted by the ANF models.

	dendrite			axon		
	v_c/ms^{-1}	$D/\mu m$	k	v_c/ms^{-1}	$D/\mu m$	k
Rattay et al. (2001)	6.15	1.68	3.66	13.1	3.36	3.89
Briaire and Frijns (2005)	4.3	5	0.86	17.1	5	3.42
Smit et al. (2010)	11.8	1.68	7.04	7.69	3.75	2.05
Frijns et al. (1994)	-	-	-	75.8	15	5.05
Smit et al. (2009)	-	-	-	43.9	15	2.93
Imennov and Rubinstein (2009)	-	-	-	15.9	2.5	6.35
Negm and Bruce (2014)	-	-	-	6.46	1.68	3.84

When considering the conduction velocities in the human ANF models, the AP propagation through the somatic region should also be taken into account. The somas have a high capacitance due to their big diameters and the nearly missing myelination. Loading it via current flow along the fiber delays the conduction of APs. This somatic delay is apparent in Fig. 4.6 which shows the responses of the human ANF models to a 100 µs cathodic current pulse, injected at the first dendritic node. The duration of the somatic delay was determined by measuring the time difference between the APs at the nodes directly before and after the soma. A delay of 305 µs was measured with the model by Rattay et al. (2001). The models of Briaire and Frijns (2005) and Smit et al. (2010) predicted shorter somatic delays of 130 µs and 240 µs, respectively.

The dendrites from Smit et al. (2010) and Rattay et al. (2001) only differ in their morphologies. Smit et al. (2010) used the same fiber diameter, but removed one of the internodes and lengthened the other internodes. This led to an increased dendritic conduction velocity as depicted in Fig. 4.5. The smallest scaling factors were determined for the ANF models with the shortest dendritic and axonal internodes (Briaire and Frijns, 2005; Smit et al., 2010). These findings give rise to the conclusion that alongside the fiber diameter the internodal length has a major impact on the conduction velocity of an ANF.

The single node model of Negm and Bruce (2014) has been extended using the morphology and internodal parameters of the dendrite as modeled by Rattay et al. (2001). Table 4.2 shows that nearly equal conduction velocities were measured in the two models. According to this, the distinct descriptions of the nodes, including different channel types, gating properties and electrical parameters, had almost no impact on the conduction velocity.

The aforementioned relationship between dendritic and axonal conduction velocities, found in feline experiments by Czéh et al. (1976), has to be reflected.

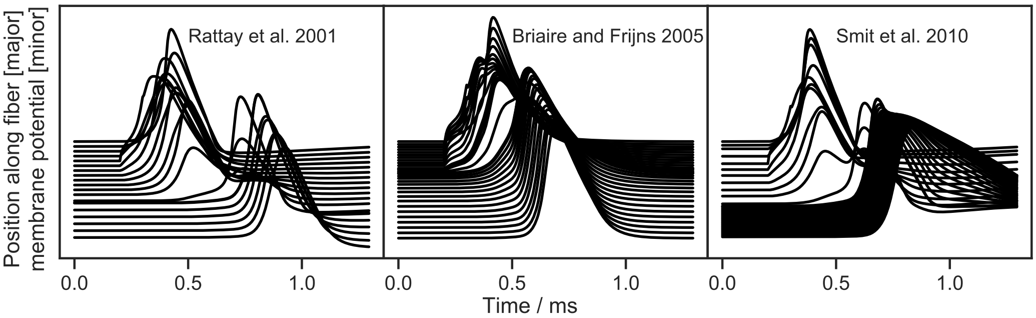

Figure 4.6 – Responses of the human ANF models by Rattay et al. (2001), Briaire and Frijns (2005) and Smit et al. (2010) to a 100 µs cathodic current pulse, injected at the first dendritic node. Each line depicts the voltage course of a single morphologic component, starting from the peripheral terminal represented by the topmost line. The lines are vertically shifted true to scale according to the compartmental distances. The visible delay in the AP propagation is a consequence of the highly capacitive soma.

They investigated mainly fibers faster than $50\,\mathrm{m\,s^{-1}}$. Thus their findings might be only applicable to fast and accordingly thick ANFs. This is not the case for the human ANF models considered in this work.

Stypulkowski and Van den Honert (1984) measured the electrically evoked compound action potential of feline auditory nerves and observed two peaks with a time difference of 200 µs. They suggested that the earlier peak arose from a direct excitation of the axon near the soma, whereas the second peak had its origin at the dendrite. Following this argumentation, the time difference of the to peaks can be used to estimate the somatic delay. Neuronal response telemetry measurements with cochlear implant patients also exhibited double-peaks with a temporal distance of 300 µs (Lai and Dillier, 2000). Using this value as a reference point the somatic delay of 305 µs as measured with the model of Rattay et al. (2001) appears very realistic. The models by Briaire and Frijns (2005) and Smit et al. (2010), however, predicted smaller delays closer to the one found for feline ANFs (Stypulkowski and Van den Honert, 1984).

4.1.3 Action potential shape

The AP shapes of the ANF models were compared by measuring the AP heights, rise and fall times. The AP height was defined as the voltage difference between the resting potential and the peak value. Rise and fall times were determined as the time periods between the maximum of an AP and 10% of that, obtained during the AP onset and ending, respectively. Figure 4.7 depicts the voltage courses of the ANF models after an excitation with a monophasic 100 µs cathodic current pulse. Both the responses to a stimulation with the models' respective current threshold and twice of that are plotted. The curves that belong to the models of Smit et al. (2009) and Smit et al. (2010) stand out due to the long falling phases. The short negative peaks, which can be observed at the onset of some of the curves, were a passive response to the cathodic stimulus. The increase of the stimulus amplitude by a factor of two was reflected in shorter latencies but had no visible impact on the AP shape. A detailed comparison of the latencies, obtained with the ANF models, was done in Sec. 4.2.3.

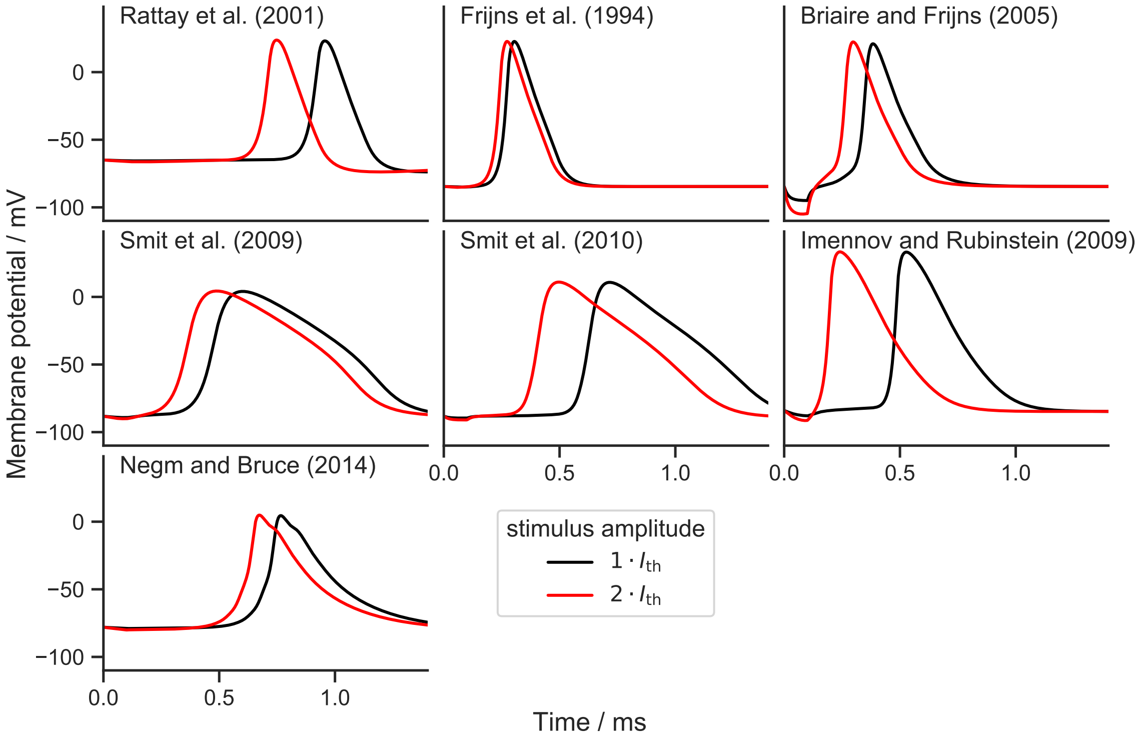

Figure 4.7 – Membrane potential responses of the ANF models to a monophasic 100 µs cathodic current pulse.

Table 4.3 lists the AP heights, rise and fall times measured with the ANF models at axonal nodes using the aforementioned stimulus. The AP heights ranged from about 82 mV to 118 mV and reached positive membrane potentials in all models, which can be seen in Fig. 4.7. The rise times were between 77 µs (Frijns et al., 1994) and 143 µs (Negm and Bruce, 2014) in all ANF models apart from the one by Smit et al. (2009) which predicted a rise time of 206 µs. The fall times of the models were distinctly higher than the respective rise times and more divergent. They ranged from 192 µs in the model of Rattay et al. (2001) to

712 µs measured with the model by Smit et al. (2010). The described AP shapes were almost constant over different pulse forms, phase durations and stimulus amplitudes.

Table 4.3 – Comparison of properties, describing the AP shape, measured with the ANF models due to a stimulation with a monophasic 100 µs cathodic current pulse with amplitude $2I_{\mathrm{th}}$.

	AP height/mV	rise time/µs	fall time/µs
Rattay et al. (2001)	87.9	104	192
Frijns et al. (1994)	107	77	213
Briaire and Frijns (2005)	104	87	229
Smit et al. (2009)	95.9	206	657
Smit et al. (2010)	107	121	712
Imennov and Rubinstein (2009)	118	85	407
Negm and Bruce (2014)	82.1	143	492

Only limited experiments with the objective to investigate the AP shape can be found in literature. Paintal (1966) measured AP rise and fall times of feline nerve fibers and fitted curves which revealed an inverse relation with the conduction velocity. The rise time curve was steep for conduction velocities below $40\,\mathrm{ms}^{-1}$ and flattened out for faster fibers. The relation with the fall times was approximated to be linear. In all fibers fall times were longer than rise times. Figure 4.8 compares these experimental results to the values measured with the ANF models. For the human ANF models, rise and fall times of both dendrite and axon are depicted to be compared.

All ANF models apart from Smit et al. (2009) predicted shorter rise times than observed by Paintal (1966) in fibers with similar conduction velocities. The rise time obtained with the model by Frijns et al. (1994) was closest to the suggested curve. Only small differences in the values were observed between the dendrite and axon within the same model.

The AP fall times of the ANF models diverged wildly. The model of Rattay et al. (2001) predicted values distinctly below the experimental line, while the axonal fall times obtained with the models by Smit et al. (2009) and Smit et al. (2010) were about twice as long as measured by Paintal (1966). The axon models of Frijns et al. (1994), Imennov and Rubinstein (2009) and the dendrite as modeled by Briaire and Frijns (2005) compared well with the experimental results.

The model parameters which affect the AP shape are discussed in the following. The rising and falling phase are defined with the time needed to charge or discharge the capacitance of a compartment. This depends firstly on the value of

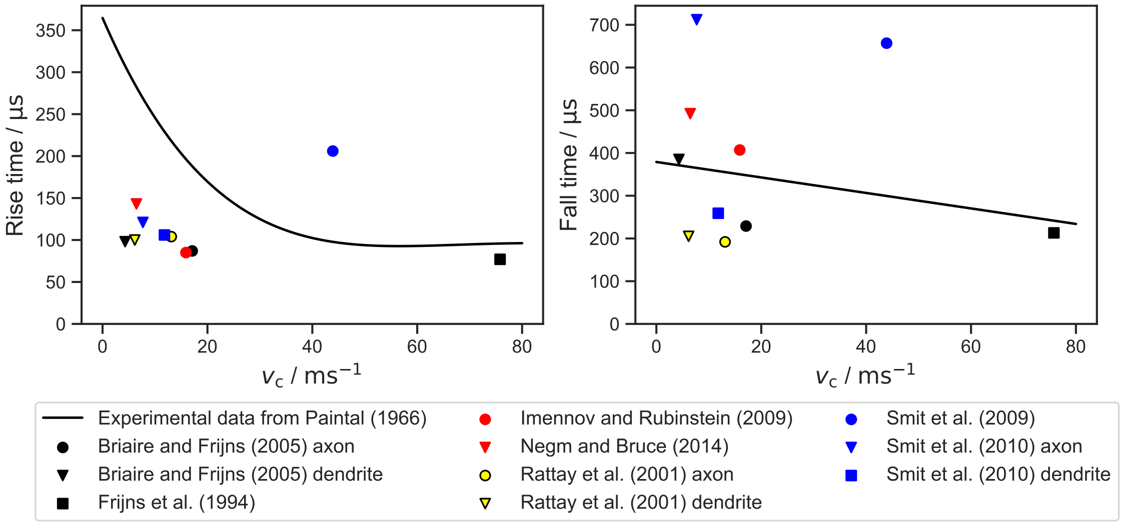

Figure 4.8 – Comparison of rise times (left) and fall times (right), measured with the ANF models, to the experimental results of Paintal (1966).

the capacitance and secondly on the gating properties of the ion channels. Conducting sodium channels depolarize the membrane. Thus the time constant of their opening process influences the rise time of an AP. Accordingly the fall time is affected by the time constant of the potassium channels which repolarize the membrane. Smit et al. (2009) and Smit et al. (2010) modeled very slow potassium channels reulting in long falling phases as shown before. The models by Imennov and Rubinstein (2009) and Negm and Bruce (2014) also included slow potassium channel species and predicted long fall times as well. The morphology of an ANF model has an impact on the AP shape as it influences the value of the capacitance. Higher capacitances lead to an increased AP height and longer rising and falling phases.

Both rise and fall time measured with the axon model by Frijns et al. (1994) were close to the experimental data. This is not surprising as the model was optimized to match with the results of Paintal (1966). Smit et al. (2009) referenced another experimental value for the fall time: according to Wesselink et al. (1999), 15 µm thick fibers have a fall time of 570 µs. However, this value was not obtained by measurements on real nerve fibers but extrapolated from results of a single node model by Sweeney et al. (1987).

4.1.4 Latency

The latency is defined as the time period between the onset of a stimulus and the peak of the resulting AP. Four monophasic cathodic stimuli differing in phase duration and stimulus amplitude were applied to the ANF models in order to elicit APs. The corresponding latencies were measured at the third peripheral node which had also been the location of the electrode. The results are listed in Tbl. 4.4 and compared to values obtained in feline experiments.

The models predicted latencies shorter than suggested in experiments for all considered stimuli. Very short latencies were measured with the models by Frijns et al. (1994) and Briaire and Frijns (2005). The values obtained with the models by Rattay et al. (2001), Smit et al. (2009) and Imennov and Rubinstein (2009) were close to the ones measured in feline nerve fibers by Cartee et al. (2000). An increase of the phase width (compare stimuli A and D) led to longer latencies in all models which goes along with the experimental data of Cartee et al. (2000) and Miller et al. (1999). Applying twice the stimulus amplitude (compare stimuli B and C) resulted in distinctly shorter latencies. The decrease of about 50%, observed in feline experiments by Van den Honert and Stypulkowski (1984) could also be measured with the model by Smit et al. (2010). All other models predicted larger relative decreases of the latency for a stimulus amplitude of $2I_{\text{th}}$ compared to I_{th}. Figure 4.7 depicts the corresponding membrane potential responses of the ANF models and visualizes the reduced latencies for a stronger stimulus current.

In general, there are two main reasons why higher stimulus amplitudes lead to shorter latencies in ANF models. Firstly, a bigger part of the fiber is stimulated and the AP arises from a more central region of the fiber. Secondly, when applying a weak stimulus around I_{th}, the initiation of an AP is delayed as it takes a while to charge the conductance sufficiently. However, the first situation does not apply here, as stimulus and measurement location were identical. Measuring the membrane potential at a more central region of the fiber will add an offset to the latencies which depends on the conduction velocity and the initial current distribution along the fiber. For a stimulation with $2I_{\text{th}}$, the passive response to the stimulus and the active response of the ion channels added up, resulting in latencies even shorter than the rise times of the models.

4.1.5 Refractory properties

The refractory properties characterize the reduced excitability of an ANF after an AP. They were measured for the models following the procedure as described by Frijns et al. (1994). Two stimuli were applied: the first one had an amplitude of $1.5I_{\text{th}}$ and elicited an AP serving as the masker for the second stimulus; the current threshold to elicit another AP with the second stimulus was determined

Table 4.4 – Comparison of latencies, measured with the ANF models, to experimental data (italiced). Four different stimuli were applied. Latencies are given in µs

	Stim. A	Stim. B	Stim. C	Stim. D
Rattay et al. (2001)	310	317	95	356
Frijns et al. (1994)	116	124	46	170
Briaire and Frijns (2005)	113	122	50	166
Smit et al. (2009)	385	371	50	387
Smit et al. (2010)	261	267	115	298
Imennov and Rubinstein (2009)	347	364	93	421
Negm and Bruce (2014)	250	258	50	302
Miller et al. (1999)	-	-	-	*650*
Van den Honert and Stypulkowski (1984)	-	*685*	*352*	-
Cartee et al. (2000)	*440*	-	-	-

A: monophasic 40 µs cathodic current pulse with amplitude I_{th}
B: monophasic 50 µs cathodic current pulse with amplitude I_{th}
C: monophasic 50 µs cathodic current pulse with amplitude $2I_{\mathrm{th}}$
D: monophasic 100 µs cathodic current pulse with amplitude I_{th}

for different inter-pulse intervals (IPIs). The IPI was defined as the time period between the onsets of the first and the second stimulus.

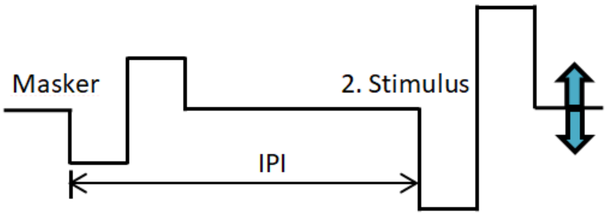

Figure 4.9 – Illustration of the stimulation scheme to determine the refractory properties of the ANF models.

Figure 4.10 depicts the refractory properties of the ANF models. The relative threshold increase of the second stimulus compared to the masker threshold is plotted over the IPIs. The resulting graphs are denoted as refractory curves in the following. A great variability among the models can be observed, but they have in common that as IPIs increase the threshold of the second stimulus approaches the masker threshold, which is marked with a dashed lines in the figure. For most models, the refractory curve as very steep at small IPIs. For the models of

Frijns et al. (1994), Imennov and Rubinstein (2009) and Negm and Bruce (2014) the threshold of the second stimulus rised within 1 µs to more than 20 times the masker threshold. The refractory curve of the model by Smit et al. (2009) is shifted to the right compared to the other curves. For IPIs of about 2 ms, the ANF models by Rattay et al. (2001) and Smit et al. (2010) predicted thresholds for the second pulse that were smaller than the masker threshold.

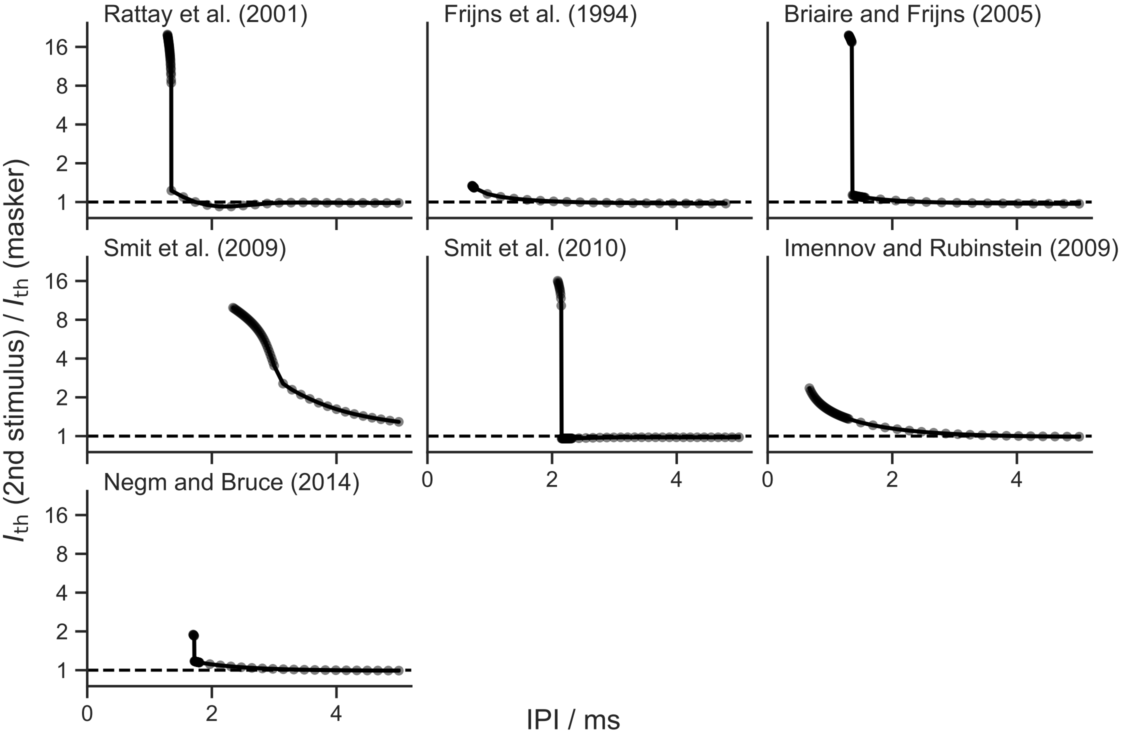

Figure 4.10 – Refractory curves of the ANF models. Both masker and second stimulus were monophasic cathodic pulses with a phase length of 50 µs. The ordinate is on a logarithmic scale.

The refractory behavior of an ANF is usually characterized with the absolute and relative refractory period. These were defined in this thesis as suggested by Wesselink et al. (1999): The absolute refractory period (ARP) was determined by the time interval between two stimuli where the second stimulus required a current amplitude of at least 4 times the masker threshold to elicit a second AP; the relative refractory period (RRP) was defined as the time interval between the two stimuli in which the threshold of the second one was increased by a factor 1.01.

Table 4.5 lists the ARPs, measured with the ANF models for four different stimuli and compares them to experimental results. Most of the models predicted longer APPs than observed in experiments. The values obtained with the models by Imennov and Rubinstein (2009) and Frijns et al. (1994) for biphasic 50 µs current pulses compared well with the data from feline nerve fibers. Imennov and Rubinstein (2009) also predicted an ARP within the experimental range for a monophasic 100 µs cathodic stimulus.

Table 4.5 – Comparison of ARPs, measured with the ANF models, to experimental data (italiced). Four different stimuli were used. ARPs are given in µs

	Stim. A	Stim. B	Stim. C	Stim. D
Rattay et al. (2001)	1355	1346	1307	1287
Frijns et al. (1994)	585	595	831	526
Briaire and Frijns (2005)	1297	1304	1312	138
Smit et al. (2009)	2956	2961	2943	3103
Smit et al. (2010)	2151	2143	2105	2139
Imennov and Rubinstein (2009)	664	664	656	479
Negm and Bruce (2014)	2148	2275	3783	1639
Miller et al. (2001)	*334*	-	-	-
Stypulkowski and Van den Honert (1984)	-	*300*	-	-
Dynes (1996)	-	-	*500-700*	-
Brown and Abbas (1990)	-	-	-	*400-500*

A: monophasic 40 µs cathodic current pulses
B: monophasic 50 µs cathodic current pulses
C: monophasic 100 µs cathodic current pulses
D: biphasic 50 µs cathodic first current pulses

Four different stimuli were applied to the ANF models to determine the RRPs. The results are listed in Tbl. 4.6 and compared to experimental data, measured in feline nerve fibers. The experiments suggest RRPs between 3 ms and 5 ms. Values within this range were predicted with the models by Imennov and Rubinstein (2009) and Negm and Bruce (2014). Shorter RRPs were measured by all other models with the exception of the model by Smit et al. (2009) which predicted long RRPs around 10 ms.

The findings of this section are now discussed. It can be assumed that the gating properties of the ion channels have a major impact on the length of the refractory periods. The inactivation process of the sodium channels specifies a time interval after an AP in which the membrane can not be depolarized again. The length of this time interval, which determines the ARP, is mainly affected by the time constant of this inactivation process. Smit et al. (2009) and Smit

Table 4.6 – Comparison of RRPs, measured with the ANF models, to experimental data (italiced). Three different stimuli were used. RRPs are given in ms

	Stim. A	Stim. B	Stim. C
Rattay et al. (2001)	1.71	1.67	1.18
Frijns et al. (1994)	2.07	2.25	1.71
Briaire and Frijns (2005)	2.33	2.49	2.42
Smit et al. (2009)	10.6	10.1	9.7
Smit et al. (2010)	2.14	2.11	1.89
Imennov and Rubinstein (2009)	3.66	3.85	3.59
Negm and Bruce (2014)	3.4	3.78	3.31
Stypulkowski and Van den Honert (1984)	*3-4*	-	-
Cartee et al. (2000)	*4-5*	-	-
Dynes (1996)	-	*5*	-
Hartmann et al. (1984b)	-	-	*5*

A: monophasic 50 µs cathodic current pulses
B: monophasic 100 µs cathodic current pulses
C: biphasic 200 µs cathodic first current pulses

et al. (2010) used a long time constant for the corresponding gating variable in their model with a maximum of 3 ms as shown in Fig. 2.9b. Therefore the predicted ARPs were about four times longer than the ones measured with the model by Imennov and Rubinstein (2009) who used a shorter time constant with a maximum of 0.8 ms. However, the sodium channels can not fully account for the length of the refractory periods. Especially the RRPs are also affected by the dynamics of the potassium channels. Open potassium channels diminish the excitability of a compartment. A long time constant leads to slowly closing channels after the repolarization and therefore to longer RRPs. The results in Tbl. 4.6 confirm this as the models that included slow potassium channels (Smit et al., 2009; Imennov and Rubinstein, 2009; Negm and Bruce, 2014) predicted the longest RRPs.

Paintal (1965) observed in feline experiments, that ARPs were longer in fibers with conduction velocities below 20 ms^{-1}. This has to be taken into account when evaluating the values, measured with the ANF models, as all models apart from the ones by Smit et al. (2009) and Frijns et al. (1994) were slower than 20 ms^{-1}.

4.1.6 Stochastic properties

Up to this point, all ANF characteristics were measured with deterministic versions of the models. Real ANFs, however, show AP timing and threshold fluctuations due to channel noise (Verveen, 1960). As described in Sec. 2.6, Imennov and Rubinstein (2009) and Negm and Bruce (2014) accounted for the stochastic behavior of ion channels using a CNT algorithm while Rattay et al. (2001) added a Gaussian noise current term. All other ANF models were deterministic. For reasons already mentioned in Chapter 3, the CNT algorithm was not implemented in this thesis. Instead, the Gaussian noise current term was added to all models in order to investigate if this simple and computationally efficient approach is sufficient to predict stochastic properties within the range of experimentally observed results.

Two properties are commonly used to describe the stochastic behavior of an ANF: The first one is the jitter, which is defined as the standard deviation of repeatedly measured latencies, and the second one is the relative spread. The latter is a measure of the threshold variability and is defined as the standard deviation of the underlying Gaussian distribution divided by its mean (van Gendt et al., 2016).

It was not possible to include exactly the same amount of stochasticity to all ANF models as the Gaussian noise current term depends on the surface areas and maximum sodium conductivities of the individual compartments (see Eq 2.12). Therefore the jitter and relative spread were measured with various values for the noise factor k_{noise} which is used to adjust how strong the channel noise is emphasized. For each k_{noise} value, the threshold measurement was repeated 100 times to calculate the relative spread; spontaneous APs, which were defined as APs occurring at 0 A, were excluded. The jitters were obtained by measuring latencies 500 times applying I_{th}; spontaneous APs, now defined as APs elicited before the onset of the stimulus, were again excluded. Monophasic 50 µs cathodic current pulses were used in each measurement. The results for the ANF models are depicted in Fig. 4.11.

All models predicted relative spreads between 0% and 30% within the considered range of k_{noise}. Increasing k_{noise} further would have resulted in even higher relative spreads. The results for the jitter were more divergent. While values of more than 100 µs were measured with the models of Rattay et al. (2001) and Smit et al. (2010), jitters smaller than 60 µs were obtained with the other ANF models for all values for k_{noise}.

Javel et al. (1987) measured relative spreads of 12% and 11% in feline ANFs using biphasic stimuli with phase durations of 200 µs and 400 µs, respectively. Smaller values between 5% and 10% were found by Miller et al. (1999) and Dynes (1996) who excited feline ANFs with monophasic pulses and phase durations of

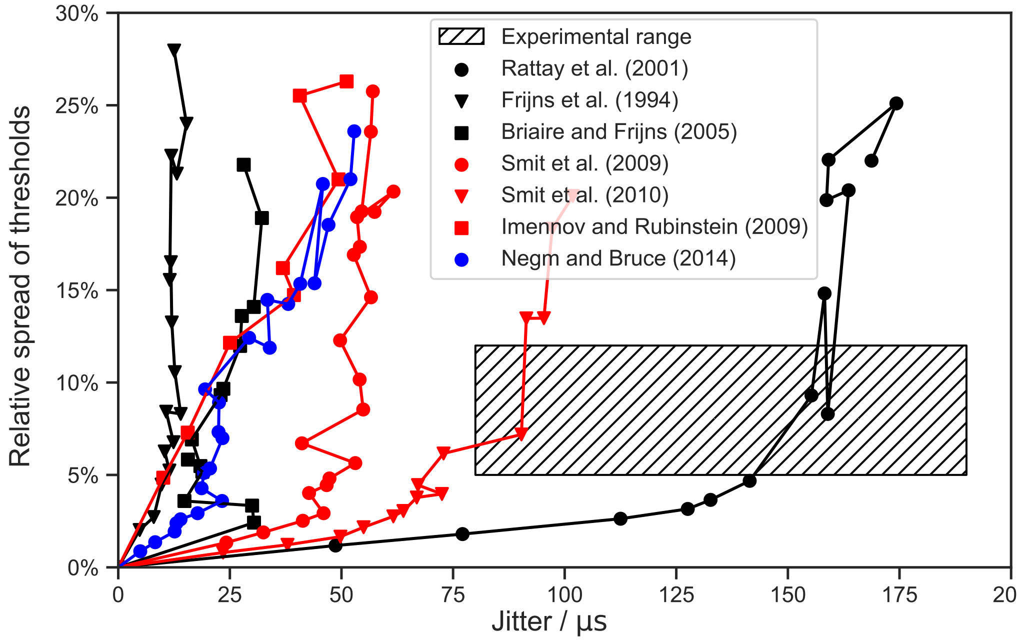

Figure 4.11 – Comparison of stochastic properties of the ANF models, when applying a Gaussian noise current term. Jitter and relative spread of threshold were measured with different values for k_{noise}. Monophasic 50 µs cathodic current pulses were used. Thresholds and latencies were measured 100 and 500 times for each datapoint, respectively.

100 µs and 40 µs. The experimentally observed jitters for a stimulation of feline ANFs with I_{th} ranged from 80 µs (Cartee et al., 2000) to 190 µs (Van den Honert and Stypulkowski, 1984).

Figure 4.11 reveals that an appropriate value for k_{noise} with both relative spread and jitter within the experimental range could only be found for the models of Rattay et al. (2001) and Smit et al. (2010). All other models predicted smaller jitters even for a high k_{noise}. This suggests that using the Gaussian noise current term might only be sufficient to simulate stochasticity in models that were optimized for this approach.

Equation 2.12 for the Gaussian noise current term implies that stochasticity is more pronounced in larger fibers and higher sodium densities. However, the evidence for the contrary was presented in Badenhorst et al. (2016), as the total number of sodium channels increases with the surface area and the sodium channel density. Thus the voltage fluctuation caused by single channels becomes less significant when compared to the total conductance and therefore the fiber becomes less stochastic.

4.1.7 Pulse-train responses and adaptation

This section investigates the spiking behavior of the ANF models for pulse-train stimulation. Responses have been measured for 300 ms pulse-trains with four different pulse rates. The poststimulus time histograms (PSTHs) in Fig. 4.12 depict the average number of APs during 10 ms time bins. Biphasic (cathodic-first) current pulses with 20 µs/phase and current amplitude I_{th} were used. Each stimulation was repeated 50 times. Stochastic responses were obtained by adding the Gaussian noise current term to all models.

For pulse trains with a rate of 400 pps, 100% firing efficiency was obtained with the models by Briaire and Frijns (2005), Frijns et al. (1994), Rattay et al. (2001) and Smit et al. (2010). Higher pulse rates led to reduced firing efficiencies in all models. Only for the model by Frijns et al. (1994), an increase in pulse rate to 800 pps came along with an increased number of AP per timebin. Other models showed a similar spiking behavior as for 400pps, except for the model of Smit et al. (2009) which predicted APs almost solely as response to the first pulse. When stimulating with a rate of 5000 pps, the models by Frijns et al. (1994) and Imennov and Rubinstein (2009) showed spiking behavior over the entire pulse train duration. For other models, only the first pulses elicited an AP. The same behavior was measured with the models by Negm and Bruce (2014), Smit et al. (2009) and Smit et al. (2010) when applying pulse trains with 2000 pps.

In several experiments on feline ANFs spiking rate adaptation has been shown. Zhang et al. (2007) measured adaptive responses to pulse trains with rates between 250 and 10000 pps. Spiking rate decrements increased as pulse rates increased. The same tendency was observed by Litvak et al. (2001) who applied pulse-train stimuli with rates of 1200 and 4800 pps. Zhang et al. (2007) and Westerman and Smith (1984) measured in feline and gerbil ANFs, that adaptation is strongest during the first 10 ms of a pulse train, but still apparent for durations of more than 100 ms. As described in Sec. 2.5, only the model of Negm and Bruce (2014) includes a mechanism to account for adaptation. Figure 4.12 shows, that for the extended version of the single node model by Negm and Bruce (2014) adaptation was measured for pulse rates of 400 pps and 800 pps. The published results for the original model, however, revealed stronger effects, which were also apparent at higher pulse rates. This discrepancy can presumably be explained by the extension of the model with a morphology and internodal parameters not optimized to be combined with the description of the nodes. Among the other ANF models, the ones by Briaire and Frijns (2005), Rattay et al. (2001) and Smit et al. (2010) also predicted adaptation in a very small degree for a stimulation with 800 pps.

Zhang et al. (2007) observed spiking rates greater than 1000 spikes per second in 30% of the investigated fibers. Such rates could not be measured with the ANF

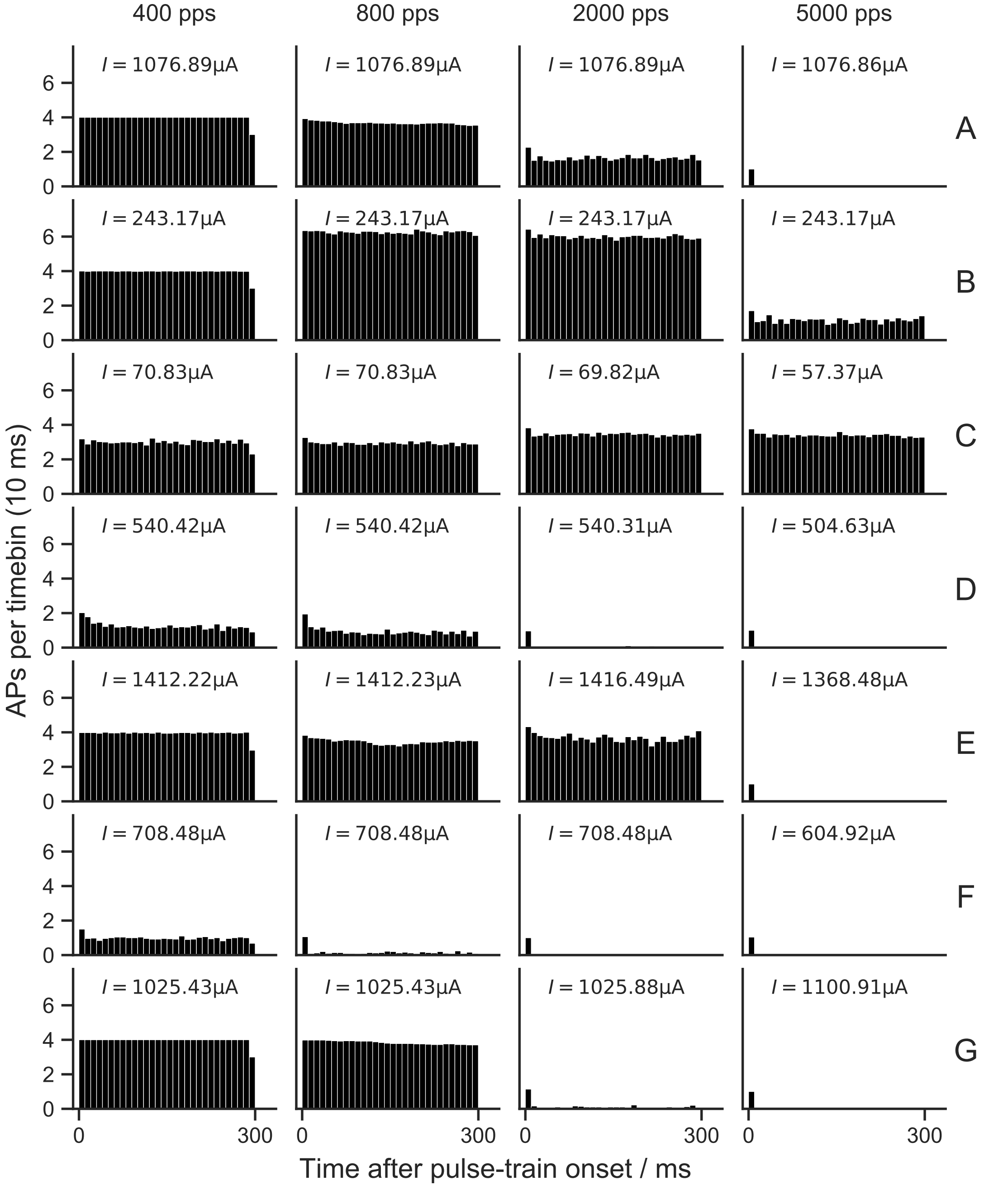

Figure 4.12 – Comparison of PSTH, measured with the ANF models. **A**: Briaire and Frijns (2005); **B**: Frijns et al. (1994); **C**: Imennov and Rubinstein (2009); **D**: Negm and Bruce (2014); **E**: Rattay et al. (2001); **F**: Smit et al. (2009); **G**: Smit et al. (2010). Biphasic (cathodic-first) current pulses with 20 µs/phase and current amplitude I_{th} were used for pulse-trains with four different pulse rates. Each stimulation was repeated 50 times. The vertical lines in the PSTHs show the average number of APs during bins with a width of 10 ms.

models when applying I_{th} as shown in Fig. 4.12. For pulse train stimulation with higher current amplitudes, the models by Frijns et al. (1994) and Imennov and Rubinstein (2009) predicted higher rates of about 1000 spikes per second. The rates obtained with the other models remained almost the same as for the stimulation with I_{th}.

4.2 ANF populations

In the previous section only the characteristics of single ANFs were discussed, which were located in a homogeneous medium and stimulated with a point electrode. This section investigates the spiking behavior of 400 ANFs, based on potential data acquired from a 3D model of the implanted human cochlea. The model was created in another study and is based on micro-CT scans of the human cochlea. It includes 400 ANFs as shown in Fig. 4.13. The extracellular potentials along each of these ANFs were calculated with the finite element method. The cochlea model provides the potential distributions for the stimulation with twelve electrodes. These are numbered according to their location along the spiral lamina in the following, beginning with 1 for the most basal electrode.

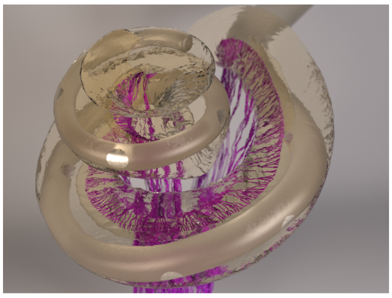

Figure 4.13 – 3D model of the implanted human cochlea including the trajectories of 400 ANFs. The model predicts extracellular potentials along each of the ANFs for twelve electrode positions.

Only four of the seven ANF models, implemented in the thesis, have been investigated in this section. The models by Frijns et al. (1994) and Smit et al. (2009) were not taken into consideration as there were newer model versions with an updated morphology including a soma (Briaire and Frijns, 2005; Smit et al., 2010). Furthermore the extended version of the single node model by Negm and Bruce (2014) was excluded.

The three-dimensional coordinates of the potentials along the ANFs, provided by the cochlea model, were converted to one dimension in a first step by only considering their respective distances. In a second step, one potential value for each compartment of the ANF models had to be found in order to calculate the activating functions. In cases where more than one potential value was located within the range of a single compartment, the mean of these potentials was used. If no value was located within the range of a compartment, the potentials directly before and after it were used for linear interpolation of the potential value at the center of the compartment. Responses of the ANF populations were then measured by applying biphasic (cathodic-first) pulses with 40 µs/phase. This includes investigations of their dynamic ranges, spiking patterns and AP latencies.

4.2.1 Dynamic ranges

The dynamic range of an ANF population was referred to the stimulus current range between the threshold value and a value for which all fibers are spiking. The threshold was defined as the minimum required current amplitude to elicit an AP with at least one of the fibers. Figure 4.14 depicts the number of spiking fibers as a function of the stimulus amplitude measured in dB above threshold. It compares the results of the ANF model populations for the twelve electrode positions.

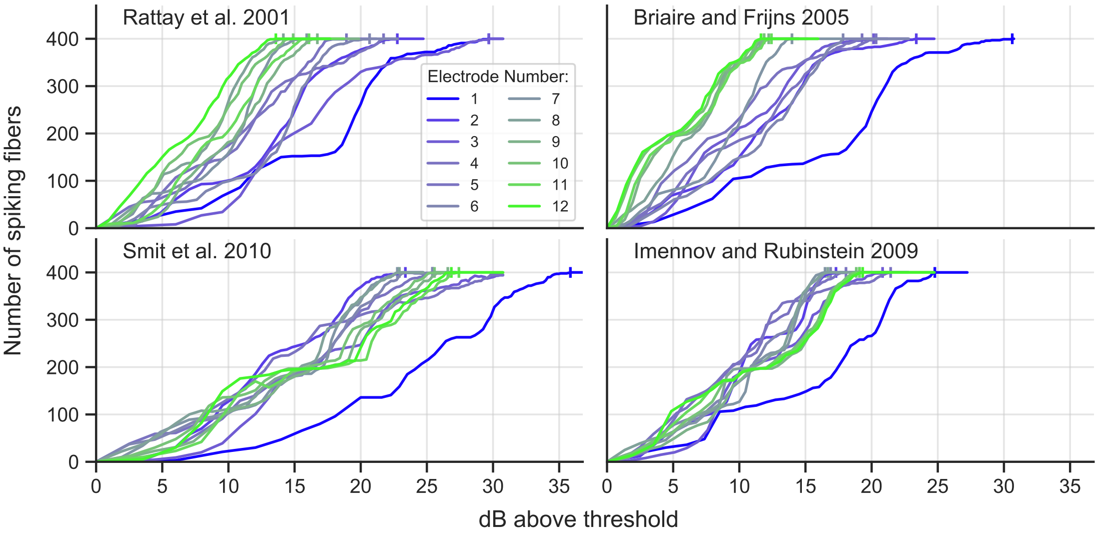

Figure 4.14 – Comparison of the dynamic ranges of the ANF model populations measured for the twelve electrode positions. The number of spiking fibers is plotted as a function of the stimulus amplitude measured in dB above threshold.

The dynamic ranges depended strongly on the location of the stimulated electrode. The biggest dynamic ranges were measured for a stimulation at the basal electrodes in all models. The maximum required current amplitudes to elicit APs with all fibers ranged from 25 dB above threshold (Imennov and Rubinstein, 2009) to more than 35 dB above threshold (Smit et al., 2010). The models by Briaire and Frijns (2005) and Rattay et al. (2001) predicted the smallest dynamic ranges for a stimulation of the most apical electrodes whereas a stimulation of intermediate electrodes led to the smallest dynamic ranges in other models.

4.2.2 Spiking patterns

This section describes and compares the spiking patterns of the ANF model populations for both pulse-train and single-pulse stimulation. Furthermore the impact of the cathodic and anodic phase on the thresholds of biphasic pulses is investigated.

Pulse-train responses

The raster plots in Fig 4.15 depict the AP timings and locations of the ANF populations for a stimulation at electrode 6 with 50 ms pulse trains and rates of 100 pps and 1000 pps. The applied stimulus amplitudes were chosen so that 25% of the fibers were spiking as a response to the first pulse. The model by Rattay et al. (2001) included stochasticity using the Gaussian noise current term; the other models were deterministic. Alongside the raster plots, the firing efficiency of the ANFs is shown, measuring the percentage of pulses which gave rise to an AP.

For both of the investigated pulse rates, mainly the ANFs near the electrode location were spiking. Interestingly, some of the fibers located at a more apical region of the cochlea elicited APs, too. This gives rise to the assumption that ANFs can be excited across neighboring turns of the spiral-shaped cochlea. For a stimulation with 100 pps, the ANF model populations predicted very regular spiking patterns where nearly all of the excited fibers had 100% firing efficiency. The synchronous spiking can be explained by the small time constants of the channel types used in the models. As these are usually shorter than 10 ms, most of the gating variables could return to their initial values before the onset of a succeeding pulse. This was different for a stimulation with 1000 pps, which led to more irregular patterns. The responses of the exited ANFs differed with regard to their firing efficiences and spike timings. The firing efficiences were smaller than 100% for all models and fibers and the maximum values ranged from 25% (Smit et al., 2009) to about 75% (Briaire and Frijns, 2005). The ANF models could not account for adaptation, i.e. their excitability did not visibly change over time.

Single pulse responses and location of first AP

Figure 4.16 depicts the spiking patterns of the ANF model populations for biphasic stimulation at three different electrode positions. The coloring marks the

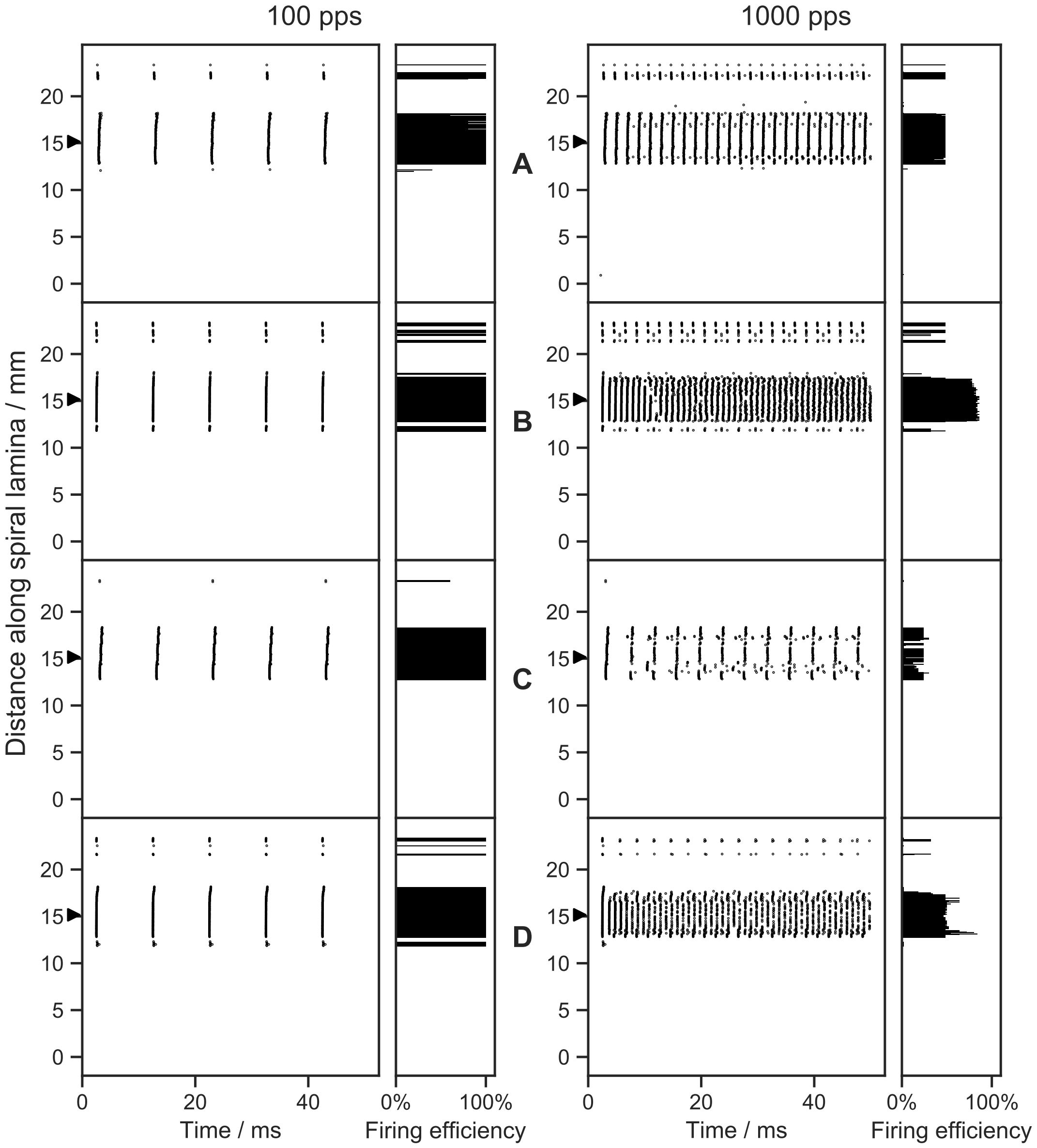

Figure 4.15 – Comparison of AP raster plots and the corresponding firing efficiency measured with the ANF models. **A**: Rattay et al. (2001); **B**: Briaire and Frijns (2005); **C**: Smit et al. (2010); **D**: Imennov and Rubinstein (2009). The raster plots show a black dot for every AP. The models were stimulated with electrode 6, applying 50 ms pulse trains with rates of 100 pps (left column) and 1000 pps (right column). The model by Rattay et al. (2001) included stochasticity, using the Gaussian noise current term.

location of the first AP along the ANFs.

The models predicted very similar spiking patterns, despite the differences in their morphologies and ion channel properties. The number of spiking ANFs increased with higher stimulus amplitudes and fiber regions with diminished or increased excitability were at the same locations of the spiral lamina in all models. This leads to the conclusion that the cochlea model with its detailed morphologic structure had the main impact on the observed spiking patterns while the description of the ANFs plays a minor role. Even the axon model by Imennov and Rubinstein (2009) with the simplified morphology predicted similar results. However, the absence of soma and dendrite led to a slightly smoother spiking pattern. The number of excited ANFs when applying a stimulus current just above the threshold at electrode 1 was distinctly smaller than for a stimulation at electrode 11. According to this, the current spread along the spiral lamina is bigger in the apical part of the cochlea, which led to the wider excitation. A likely explanation for this observation is the smaller diameter of the apical turn compared to the basal one. There are gaps in the spiking patterns, for example between a distance of 15 mm and 20 mm along the spiral lamina for a stimulation at electrode 1. The presence of such gaps reveals that less excitable fiber regions can be a consequence of the cochlear morphology and are not necessarily caused by missing or degenerated neurons.

The coloring in Fig. 4.16 shows that the location of the first AP moved to more central regions of the ANFs for increasing distances to the stimulating electrode, for decreasing stimulus amplitudes and for a stimulation closer to the base of the cochlea. The location of the first AP is a good indicator for the position of the highest activating function along an ANF.

Spiking patterns of cathodic, anodic and biphasic pulses

As mentioned, the responses of the ANF populations were measured applying biphasic pulses (cathodic-first) with 40 µs/phase. For a further analyses of the spiking patterns shown in Fig. 4.16, the impact of the two phases of the biphasic pulse is investigated in this section. Therefore the thresholds for cathodic, anodic and biphasic stimulation are compared for three electrode locations in Fig. 4.17.

As already shown before, the spiking patterns for biphasic pulses were similar for all ANF models. Interestingly the results for monophasic stimulation differed among models especially when applying anodic pulses.

The thresholds for biphasic pulses obtained with the models by Rattay et al. (2001), Smit et al. (2010) and Imennov and Rubinstein (2009) followed the patterns of the cathodic stimulation but were higher. The patterns for anodic stimulation obtained with the model by Smit et al. (2010) were similar for all electrode locations and differed a lot from the thresholds measured with the other models.

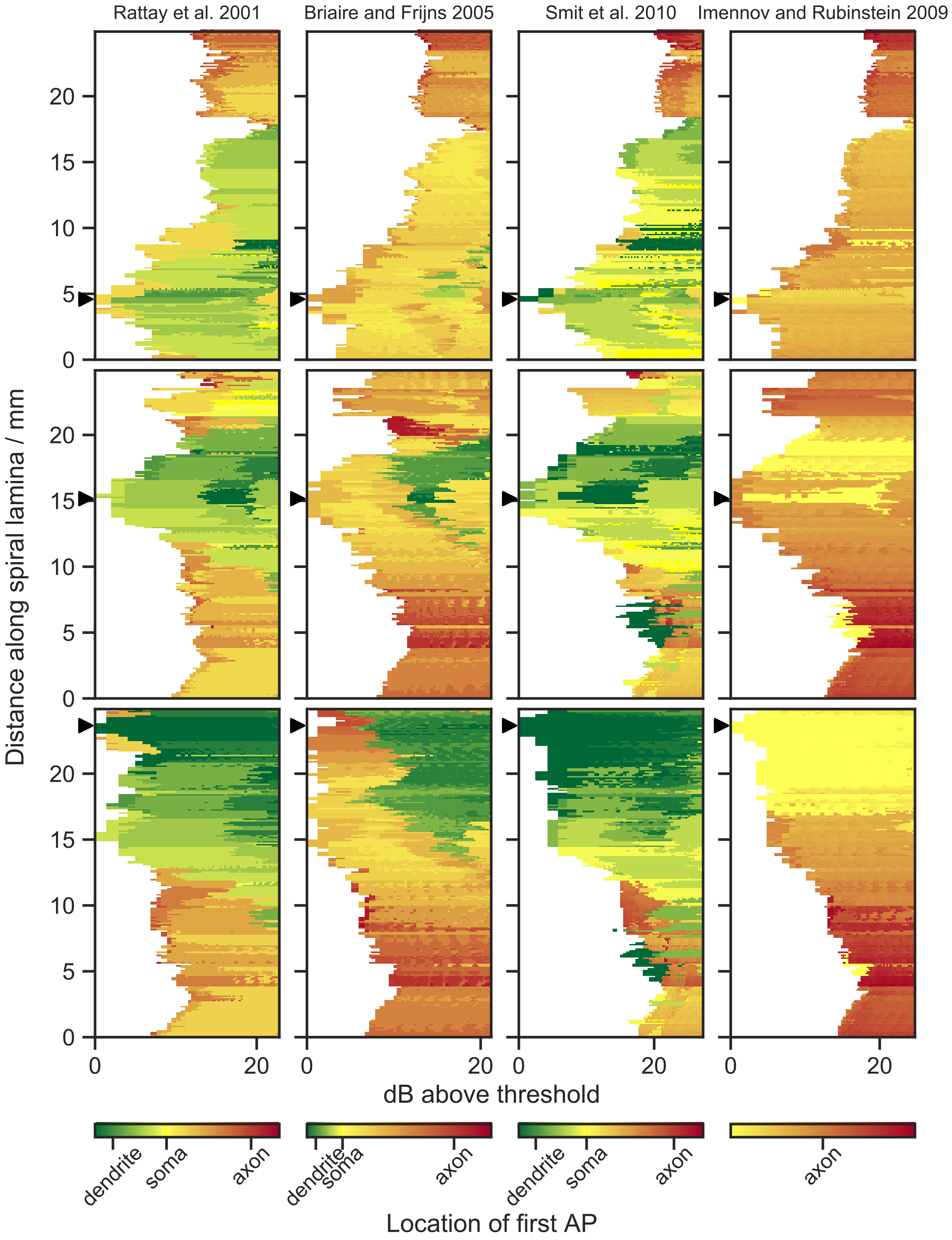

Figure 4.16 – Comparison of spiking patterns for biphasic pulses. The colors mark the location of the first AP along the ANFs. Each row depicts the responses for a certain electrode position, marked with the arrow on the ordinates. Topmost row: electrode 1; middle row: electrode 6; bottommost row: electrode 12.

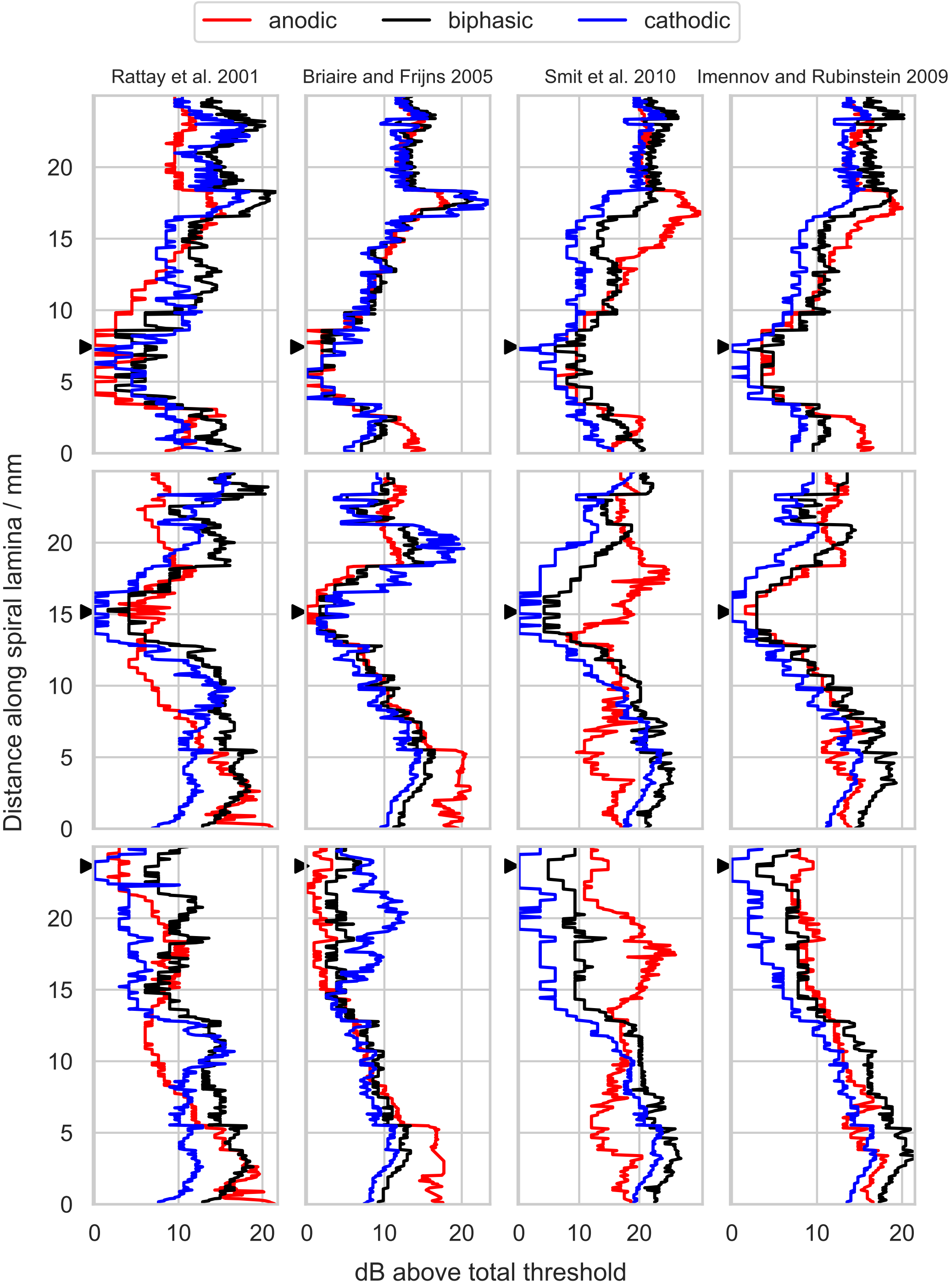

Figure 4.17 – Comparison of the spiking patterns for anodic, cathodic and biphasic stimulation, measured with the ANF model populations. Each row depicts the responses for a certain electrode position, marked with the arrow on the ordinates. Topmost row: electrode 2; middle row: electrode 6; bottommost row: electrode 12.

For an anodic stimulation at electrodes 6 and 12, the responses of the model by Smit et al. (2010) were approximately mirror-inverted patterns of the results for cathodic and biphasic pulses.

The responses for biphasic stimulation, measured with the model by Briaire and Frijns (2005) always followed the pattern of the monophasic pulse with the lower threshold. At most distances along the spiral lamina cathodic pulses led to lower thresholds, but for example between 15 mm and 25 mm and a stimulatioin with electrode 12, the biphasic pulse followed the pattern of the anodic stimulus.

4.2.3 Latency

Figure 4.18 depicts the same spiking patterns for electrode 6 as shown in Fig. 4.16, but now the colors mark the AP latencies. These were measured at the axonal terminals of the ANFs.

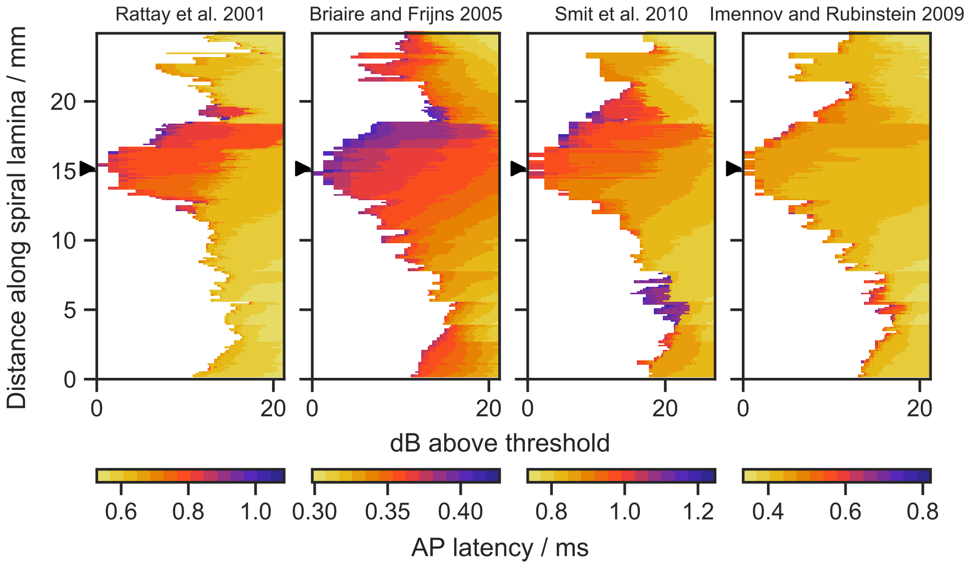

Figure 4.18 – Comparison of spiking patterns for biphasic pulses, applied at electrode 6. The colors mark the AP latencies, measured at the end of the axons.

The results of all models follow the same patterns. The latencies became shorter for increasing distances to the electrode location and for higher stimulus amplitudes. The latter observation can be explained with the fact that a bigger part of the ANFs is excited when applying higher currents. Thus the APs initiate from a more central region of the fibers which leads to shorter latencies. Fig. 4.16 has shown that the location of the first AP also moved to a more central region of the ANFs for increasing distances to the electrode.

Chapter 5

Summary

In this study seven biophysical ANF models have been implemented and evaluated. In the first step, the major characteristics of single fibers were measured and compared with experimentally obtained data. In the second step, the spiking behavior of 400 ANFs, stimulated with a model of the implanted human cochlea, was investigated. This section summarizes the results and points out the limitations of the models.

All ANF models predicted values for τ_{chr} within the range of experimental results. Applying anodic stimuli resulted in higher values for I_{rh} than observed for cathodic pulses whereas τ_{chr} differed only slightly among polarities. The thresholds for pulse train stimulation remained constant for pulse rates up to 2000 pps and train durations longer than 1 ms. Most models predicted smaller thresholds for pulse rates higher than 2000 pps. The maximum reduction of up to 3 dB was obtained with the model by Imennov and Rubinstein (2009). However, none of the models was able to account for pulse-train integration in a comparable range with the experimental results. Hardly any differences to the single pulse thresholds were measured with the models by Frijns et al. (1994) and Briaire and Frijns (2005).

The scaling factors, which describe the ratio of conduction velocity and outer fiber diameter, were within 20% of the experimental results for most of the models. Only the scaling factors for the dendrite of the model by Briaire and Frijns (2005) and the axons as modeled by Smit et al. (2009) and Smit et al. (2010) were considerably smaller than the experimentally observed values.

Neural response telemetry measurements with cochlear implant patients suggested a somatic delay of 300 µs for human ANFs (Lai and Dillier, 2000). Therefore the delay of 305 µs measured with the model by Rattay et al. (2001) is very realistic. The models by Briaire and Frijns (2005) and Smit et al. (2010) predicted smaller delays close to the ones found for feline ANFs (Stypulkowski and Van den Honert, 1984).

The AP heights, obtained with the models, ranged from 82 mV to 118 mV. Paintal (1966) measured AP rise and fall times in feline nerve fibers and found an inverse relation with the conduction velocity. All ANF models except for the one by Smit et al. (2009) predicted shorter rise times than observed by Paintal (1966) in fibers with similar conduction velocities. The measured fall times diverged wildly and ranged from 192 µs (Rattay et al., 2001) to 712 µs (Smit et al., 2010). Both rise and fall time obtained with the axon model by Frijns et al. (1994) compared well with the experimental values.

For a stimulation with I_{th}, all models predicted latencies shorter than observed in feline measurements, although the values obtained with the models by Rattay et al. (2001), Smit et al. (2009) and Imennov and Rubinstein (2009) were close to the experimental results. In accordance with experimental findings, latencies were smaller for higher stimulus amplitudes and shorter stimulus durations.

Measurements on feline ANFs suggest ARPs between 300 µs and 500 µs and about ten times longer RRPs. Most of the models overestimated the ARPs and underestimated the RRPs. Only the ones by Frijns et al. (1994) and Imennov and Rubinstein (2009) predicted ARPs as short as experimentally observed. The RRPs measured with models by Imennov and Rubinstein (2009) and Negm and Bruce (2014) compared well with the experimental results, as against the model of Smit et al. (2009) which predicted higher values of more than 10 ms.

The Gaussian noise current term as described by Rattay et al. (2001) was added to all ANF models in order to measure the jitter and relative spread of thresholds. An appropriate value for k_{noise} with both relative spread and jitter within the experimental range could only be found for the models of Rattay et al. (2001) and Smit et al. (2010). All other models predicted smaller jitters even for a high k_{noise}.

For pulse train stimulation with rates higher than 2000 pps, ongoing spiking behavior was only observed for the models by Imennov and Rubinstein (2009) and Frijns et al. (1994). Furthermore, these models were the only ones which predicted spike rates as high as shown in experiments when applying stimulus currents bigger than I_{th}. None of the ANF models could account for adaptation in a comparable range with the experimental results.

The spiking patterns obtained for a stimulation of ANF populations revealed an excitation of ANFs across neighboring turns of the cochlea. The current spread along the spiral lamina was bigger in apical regions of the cochlea than in basal ones. The nerve fiber location of the first AP moved to a more central part for increasing distances to the stimulating electrode. The thresholds for cathodic pulses followed the patterns of the biphasic stimulation but were lower. The spiking patterns for anodic pulses differed considerably among models. The AP latencies became shorter for increasing distances to the electrode location and for higher stimulus amplitudes.

In conclusion, none of the models was capable of predicting all investigated ANF characteristics within the experimental range. While the results for single pulse stimulation usually compared well with the experimental data, the models could not appropriately account for temporal effects as pulse-train integration or adaptation. The spiking patterns measured with the ANF populations were helpful to gain a more thorough understanding of how the auditory nerve responds to electrical stimulation inside the cochlea. The ANF models implemented and evaluated in the course of this thesis are a valuable basis for further tests and can serve as a starting point for the creation of improved ANF models.

Chapter 6

Outlook

The results of this thesis revealed that the capability of contemporary models to predict realistic ANF responses is limited. Therefore this section discusses ideas how ANF models could be improved in future.

In order to obtain a description of the human ANF morphology, the axon model by Imennov and Rubinstein (2009) has to be extended by including dendrite and soma. The extension of the axon model by Frijns et al. (1994) as done by Briaire and Frijns (2005) can serve as an example. However, it has been shown in this work that modifications of the morphology also alter ANF properties as the conduction velocity, refractory properties and pulse-train responses. Thus further optimizations apart from the extension of the morphology might be necessary.

Rattay et al. (2001) included stochasticity to their model by adding a Gaussian noise current term which was directly proportional to the square root of the maximum sodium conductivity and the membrane surface area (see Eq. 2.12). Badenhorst et al. (2016) described, that the inverse relation is more realistic. Thus it has to be tested how the models predict stochastic properties as the jitter and relative spread after a modification of the noise term as suggested by Badenhorst et al. (2016).

The ANF models have to be extended with a mechanism capable of predicting long-term effects as adaptation. At the current state of research there is no agreement on the cause of the adaptive behavior in real ANFs. However, ion channels with slow dynamics as the KLT and HCN channels are a likely explanation (Negm and Bruce, 2008). These channel types have been included to a single node model (Negm and Bruce, 2014) but no results for their application in ANF models have been published until now. The results of this thesis have shown that an extension of the single node model by Negm and Bruce (2014) with an arbitrary morphology is not appropriate to create an ANF model which can replicate adaptive behavior. Simply adding the KLT and HCN channels to existing ANF models is also not sufficient as the inclusion of additional channel types alters the entire spiking behavior of a model.

Some of the methodes used in the ANF models have to be reconsidered. Imennov and Rubinstein (2009) split the internodes in their axon model into nine equally spaced segments in order to approximate the solution of the continous cable equation more closely. Dekker et al. (2014) have shown that the internodal segmentation scheme influences several model properties as AP shape, conduction velocity, current thresholds and the absolute refractory period. The determinant is not the number of segments N but the length λ of the internodal segments adjacent to the nodes. If λ is larger than 10 µm, the model outcomes become almost independent of N. So the approximation of the continuous cable equation is best for a small λ ($<<$ 10 µm) and high values for N. According to the findings by Dekker et al. (2014), the use of nine equally spaced segments in the model by Imennov and Rubinstein (2009) is not appropriate. The value for λ is 25 µm, so there is hardly a benefit from additional segments.

Only a selection of ANF characteristics was investigated in this thesis. Further measurements have to be done in future works to enhance our understanding of how ANFs respond to electrical stimulation. Especially informative results can be obtained for a stimulation of the models with the potential data acquired from the cochlea model.

List of Figures

2.1 Scheme of the human ANF morphology as used by Rattay et al. (2001). The blue color denotes myelinated components. 5

2.2 Scheme of the human ANF morphology as used by Smit et al. (2010) 6

2.3 Scheme of the human ANF morphology as used by Briaire and Frijns (2005) 6

2.4 Scheme of the morphology as used for the axon models 6

2.5 Electrical equivalent circuit diagram of an active compartment in between two passive compartments. The electric components of the active compartment are: voltage-dependend membrane conductivities g_{Na} and g_{K} of the sodium and potassium channels; constant conductivity g_{L} for the leakage current; corresponding Nernst potentials E_{Na}, E_{K} and E_{L}; capacitance C_{m}; axoplasmatic resistance to the neighbors $R_{\mathrm{a}}/2$. The external and internal potentials at compartment n are given as $V_{\mathrm{e,n}}$ and $V_{\mathrm{i,n}}$, respectively. The passive compartments are described with the capacitance C_{m} and conductance G_{m} 7

2.6 Double cable structure of an internode as used by Smit et al. (2009). The myelin layers are characterized by the conductivity g_{my} and the capacity c_{my}. The corresponding parameters for the axolemma are g_{mem} and c_{mem}. 8

2.7 Electrical equivalent circuit diagram of an active compartment as used in the stochastic models by Imennov and Rubinstein (2009) and Negm and Bruce (2014). γ_{Na} and γ_{K} are the single-channel conductances of sodium and potassium, which are depicted representatively for other ion species used in the models. $X_{\mathrm{i}}^{\mathrm{Na}}$ and $X_{\mathrm{i}}^{\mathrm{K}}$ are the corresponding stochastic single-channel states, which can be open or closed. The rest of the parameters was explained in Fig. 2.5. 10

2.8 Gating properties of the sodium and potassium channels in the model by Rattay et al. (2001). 12

2.9 Gating properties of the sodium and potassium channels in the model by Smit et al. (2009). The peaks of τ_m and τ_mp are not visible due to the scaling. The maximum value of τ_m is 0.03 ms and reached at 25 mV. τ_mp has a maximum of 0.075 ms for a membrane potential of 45 mV. 13
2.10 Gating properties of the sodium and potassium channels as proposed by Schwarz and Eikhof (1987) and adopted by Frijns et al. (1994) and Briaire and Frijns (2005). 15
2.11 Gating properties of the sodium and potassium channels in the model by Imennov and Rubinstein (2009). 15
2.12 Gating properties of the sodium and potassium channels in the single node model by Negm and Bruce (2014). 16
2.13 Gating properties of the KLT and HCN channels in the model by Negm and Bruce (2014). 18

4.1 Comparison of strength-duration curves for monophasic cathodic (left) and anodic (right) stimuli. The abscissa is in log-scale for a better discriminability of the curves. 23
4.2 Activating function along an axon for A: cathodic and B: anodic stimulation. The simplified case of a constant axoplasmatic resistance and a straight fiber was assumed. 25
4.3 Thresholds as a function of pulse rate (left column) and pulse-train duration (right column). **A**: Briaire and Frijns (2005); **B**: Frijns et al. (1994); **C**: Imennov and Rubinstein (2009); **D**: Negm and Bruce (2014); **E**: Rattay et al. (2001); **F**: Smit et al. (2009); **G**: Smit et al. (2010). Biphasic cathodic first 45 µs pulses with an inter-phase gap of 8 µs were used. 26
4.4 Measurement scheme for dendritic conduction velocities. 27
4.5 Comparison of conduction velocities v_c, measured with the ANF models to experimental data. The velocities are plotted against the models respective outer diameters D. 28
4.6 Responses of the human ANF models by Rattay et al. (2001), Briaire and Frijns (2005) and Smit et al. (2010) to a 100 µs cathodic current pulse, injected at the first dendritic node. Each line depicts the voltage course of a single morphologic component, starting from the peripheral terminal represented by the topmost line. The lines are vertically shifted true to scale according to the compartmental distances. The visible delay in the AP propagation is a consequence of the highly capacitive soma. 30
4.7 Membrane potential responses of the ANF models to a monophasic 100 µs cathodic current pulse. 31

4.8 Comparison of rise times (left) and fall times (right), measured with the ANF models, to the experimental results of Paintal (1966). 33

4.9 Illustration of the stimulation scheme to determine the refractory properties of the ANF models. 35

4.10 Refractory curves of the ANF models. Both masker and second stimulus were monophasic cathodic pulses with a phase length of 50 µs. The ordinate is on a logarithmic scale. 36

4.11 Comparison of stochastic properties of the ANF models, when applying a Gaussian noise current term. Jitter and relative spread of threshold were measured with different values for k_{noise}. Monophasic 50 µs cathodic current pulses were used. Thresholds and latencies were measured 100 and 500 times for each datapoint, respectively. 40

4.12 Comparison of PSTH, measured with the ANF models. **A**: Briaire and Frijns (2005); **B**: Frijns et al. (1994); **C**: Imennov and Rubinstein (2009); **D**: Negm and Bruce (2014); **E**: Rattay et al. (2001); **F**: Smit et al. (2009); **G**: Smit et al. (2010). Biphasic (cathodic-first) current pulses with 20 µs/phase and current amplitude I_{th} were used for pulse-trains with four different pulse rates. Each stimulation was repeated 50 times. The vertical lines in the PSTHs show the average number of APs during bins with a width of 10 ms. 42

4.13 3D model of the implanted human cochlea including the trajectories of 400 ANFs. The model predicts extracellular potentials along each of the ANFs for twelve electrode positions. 43

4.14 Comparison of the dynamic ranges of the ANF model populations measured for the twelve electrode positions. The number of spiking fibers is plotted as a function of the stimulus amplitude measured in dB above threshold. 44

4.15 Comparison of AP raster plots and the corresponding firing efficiency measured with the ANF models. **A**: Rattay et al. (2001); **B**: Briaire and Frijns (2005); **C**: Smit et al. (2010); **D**: Imennov and Rubinstein (2009). The raster plots show a black dot for every AP. The models were stimulated with electrode 6, applying 50 ms pulse trains with rates of 100 pps (left column) and 1000 pps (right column). The model by Rattay et al. (2001) included stochasticity, using the Gaussian noise current term. 46

4.16 Comparison of spiking patterns for biphasic pulses. The colors mark the location of the first AP along the ANFs. Each row depicts the responses for a certain electrode position, marked with the arrow on the ordinates. Topmost row: electrode 1; middle row: electrode 6; bottommost row: electrode 12. 48
4.17 Comparison of the spiking patterns for anodic, cathodic and biphasic stimulation, measured with the ANF model populations. Each row depicts the responses for a certain electrode position, marked with the arrow on the ordinates. Topmost row: electrode 2; middle row: electrode 6; bottommost row: electrode 12. 49
4.18 Comparison of spiking patterns for biphasic pulses, applied at electrode 6. The colors mark the AP latencies, measured at the end of the axons. 50

List of Tables

2.1 Overview of models implemented in this study. 4

4.1 Comparison of rheobase I_{rh} and chronaxie τ_{chr} of the ANF models for monophasic cathodic and anodic stimulation. 24
4.2 Comparison of conduction velocities, outer diameters and scaling factors predicted by the ANF models. 29
4.3 Comparison of properties, describing the AP shape, measured with the ANF models due to a stimulation with a monophasic 100 µs cathodic current pulse with amplitude $2I_{\mathrm{th}}$. 32
4.4 Comparison of latencies, measured with the ANF models, to experimental data (italiced). Four different stimuli were applied. Latencies are given in µs 35
4.5 Comparison of ARPs, measured with the ANF models, to experimental data (italiced). Four different stimuli were used. ARPs are given in µs 37
4.6 Comparison of RRPs, measured with the ANF models, to experimental data (italiced). Three different stimuli were used. RRPs are given in ms 38

Bibliography

Adamson, C., Reid, M., Mo, Z., Bowne-English, J., and Davis, R. (2002). Firing features and potassium channel content of murine spiral ganglion neurons vary with cochlear location. *Journal of comparative neurology.*

Armstrong, D., Harvey, R., and Schild, R. F. (1973). The Spatial Organisation of Climbing Fibre Branching in the Cat Cerebellum. *Experimental Brain Research*, 58:40–58.

Badenhorst, W., Hanekom, T., and Hanekom, J. J. (2016). Development of a voltage-dependent current noise algorithm for conductance-based stochastic modelling of auditory nerve fibres. *Biological Cybernetics*, 110(6):403–416.

Baylor, D. A. and Nicholls, J. (1969). Changes in extracellular potassium concentration produced by neuronal activity in the central nervous system of the leech. *Journal of Physiology*, pages 555–569.

BeMent, S. L. and Ranck, J. B. (1969). Quantitative Study Central of Electrical Stimulation Fibers of Myelinated. *Experimental Neurology*, 170:147–170.

Blight, A. R. (1985). Computer simulation and afterpotentials in axons: the case for a lower resistance myelin sheath. *Neuroscience*, 15(1):13–31.

Boyd, I. and Kalu, K. (1979). Scaling factor relating conduction velocity and diameter for myelinated afferent nerve fibres in the cat hind limb. *Journal of Physiology*, (1979):277–297.

Briaire, J. J. and Frijns, J. H. (2005). Unraveling the electrically evoked compound action potential. *Hearing Research*, 205(1-2):143–156.

Brown, C. J. and Abbas, P. J. (1990). Electrically evoked whole-nerve action potentials : Parametric data from the cat. *Acoustical Society of America*, 2205.

Caldwell, J. H., Schaller, K. L., Lasher, R. S., Peles, E., and Levinson, S. R. (2000). Sodium channel Nav1.6 is localized at nodes of Ranvier, dendrites, and synapses. *Proceedings of the National Academy of Sciences*, 97(10):5616–5620.

Carlyon, R. P., Deeks, J. M., and McKay, C. M. (2015). Effect of Pulse Rate and Polarity on the Sensitivity of Auditory Brainstem and Cochlear Implant Users to Electrical Stimulation. *JARO - Journal of the Association for Research in Otolaryngology*, 668:653–668.

Cartee, L. A., Van Den Honert, C., Finley, C. C., and Miller, R. L. (2000). Evaluation of a model of the cochlear neural membrane. I. Physiological measurement of membrane characteristics in response to intrameatal electrical stimulation. *Hearing Research*, 146(1-2):143–152.

Chen, C. (1997). Hyperpolarization-activated current (Ih) in primary auditory neurons. *Hearing Research*, 110:179–190.

Chiu, S. Y., Ritchie, J. M., Rogart, B., and Stagg, D. (1979). A quantitative description of membrane currents in rabbit myelinated nerve. *Journal of Physiology*, pages 149–166.

Chow, C. C. and White, J. A. (1996). Spontaneous action potential fluctuations due to channel fluctuations. *Biophysical Journal*, 71(December):3013–3021.

Czéh, G., Kudo, N., and Kuno, M. (1976). Membrane properties and conduction velocity in sensory neurones follwing central or peripheral axotomy. *Journal of Physiology*, pages 757–767.

Dekker, D. M. T., Briaire, J. J., and Frijns, J. H. M. (2014). The impact of internodal segmentation in biophysical nerve fiber models. *Journal of Computational Neuroscience*, pages 307–315.

Dynes, S. B. S. (1996). *Discharge Characteristics of Auditory Nerve Fibers for Pulsatile Electrical Stimuli.pdf*. PhD thesis, Massachusetts institute of technology.

Frankenhaeuser, B. and Huxley, A. F. (1964). The action potential in the myelinated nerve fibre of Xenopus laevis as computed on the basis of voltage clamp data. pages 302–315.

Frijns, J. H., Briaire, J. J., and Schoonhoven, R. (2000). Integrated use of volume conduction and neural models to simulate the response to cochlear implants. *Simulation Practice and Theory*, 8(1-2):75–97.

Frijns, J. H. M., Desnoo, S. L., and Schonhooven, R. (1995). Potential distribution and neural excitation patterns in rotationally symmetrical model of the elctrically stimulated cochlea. 87(1-2):170–186.

Frijns, J. H. M., Mooij, J., and Kate, J. H. (1994). A Quantitative Approach to Modeling Mammalian Myelinated Nerve Fibers for Electrical Prosthesis Design. *IEEE Trnsactions on Biomedical Engineering*, 41(6):556–566.

Gillespie, D. (1977). Exact stochastic simulation of coupled chemical reactions. *J. of Physical Chemistry*, 81(25):2340–2361.

Goodman, D. F. M. and Brette, R. (2009). The Brian simulator. 3(2):192–197.

Hartmann, R., Topp, G., and Klinke, R. (1984a). Discharge patterns of cat primary auditory fibers with electrical stimulation of the cochlea. *Hearing Research*, 13:47–62.

Hartmann, R., Topp, G., and Klinke, R. (1984b). Discharge patterns of cat primary auditory nerve fibers with elecrical stimulation of the cochlea. *Hearing Research*, 13(1):47–62.

Hodgkin, A. L. and Huxley, A. F. (1952). A quantitative description of membrane current and its application to conduction and excitation in nerve. pages 500–544.

Honmou, O., Utzschneider, D. A., Rizzo, M. A., Bowe, C. M., Waxman, S. G., and Kocsis, J. D. (1994). Delayed Depolarization and Slow Sodium Currents in Cutaneous Afferents. *Journal of Neurophysiology*, 21(6):531–536.

Hursh, J. (1939). Conduction velocity and diameter of nerve fibers.

Imennov, N. S. and Rubinstein, J. T. (2009). Stochastic population model for electrical stimulation of the auditory nerve. *IEEE Transactions on Biomedical Engineering*, 56(10):2493–2501.

Intyre, C. C. M. C., Richardson, A. G., Grill, W. M., Cameron, C., Richardson, A. G., and Warren, M. (2001). Modeling the Excitability of Mammalian Nerve Fibers: Influence of Afterpotentials on the Recovery Cycle. *Journal of Neurophysiology*, pages 995–1006.

Javel, E. and Shepherd, R. K. (2001). Electrical stimulation of the auditory nerve. *Hearing Research*, 140(2000):45–76.

Javel, E., Tong, Y., Shepherd, R. K., and Clark, G. M. (1987). Responses of cat auditory nerve fibers ot biphasic electrical current pulses. *Physiology and Psychophysics.*

Lai, W. K. and Dillier, N. (2000). A Simple Two-Component Model of the Electrically Evoked Compound Action Potential in the Human Cochlea. *Zurich Open Repository and Archive*, 5:333–345.

Liberman, M. and Oliver, M. (1984). Morphometry of intracellularly labeled neurons of the auditory nerve: correlations with functional properties. *Journal of Computational Neuroscience.*

Limb, C. J. and Roy, A. T. (2014). Technological, biological, and acoustical constraints to music perception in cochlear implant users. *Hearing Research*, 308:13–26.

Litvak, L., Delgutte, B., and Eddington, D. (2001). Auditory nerve fiber responses to electric stimulation : Modulated and unmodulated pulse trains. *Acoustical Society of America*, 368(2001).

McIntyre, C. C., Richardson, A. G., and Grill, W. M. (2002). Modeling the Excitability of Mammalian Nerve Fibers: Influence of Afterpotentials on the Recovery Cycle. *Journal of Neurophysiology*, 87(2):995–1006.

Miller, C. A., Abbas, P. J., and Robinson, B. K. (2001). Response Properties of the Refractory Auditory Nerve Fiber. *Journal of the Association for Research in Otolaryngology*, 2(3):216–232.

Miller, C. A., Abbas, P. J., and Rubinstein, J. T. (1999). An empirically based model of the electrically evoked compound action potential. *Hearing Research*, 135(1-2):1–18.

Miller, C. A., Hu, N., Zhang, F., Robinson, B. K., and Abbas, P. J. (2008). Changes across time in the temporal responses of auditory nerve fibers stimulated by electric pulse trains. *JARO - Journal of the Association for Research in Otolaryngology*, 9(1):122–137.

Mino, H., Rubinstein, J. T., and White, J. A. (2002). Comparison of algorithms for the simulation of action potentials with stochastic sodium channels. *Annals of Biomedical Engineering*, 30(4):578–587.

Mo, Z.-L., Adamson, C. L., and Davis, R. L. (2002). Dendrotoxin-sensitive K + currents contribute to accommodation in murine spiral ganglion neurons. *The Journal of Physiology*, 542(3):763–778.

Mo, Z. L. and Davis, R. L. (1997). Heterogeneous voltage dependence of inward rectifier currents in spiral ganglion neurons. *Journal of neurophysiology*, 78(6):3019–27.

Motz, H. and Rattay, F. (1986). A study of the application of the hodgkin huxley and the frankenhaeuser huxley model for electrostimulation of the acoustic nerve. *Neuroscience*, 18(3):699–712.

Negm, M. H. and Bruce, I. C. (2008). Effects of I_h and I_KLT on the response of the auditory nerve to electrical stimulation in a stochastic Hodgkin-Huxley model. *IEEE Engineering in Medicine and Biology Society*, pages 5539–5542.

Negm, M. H. and Bruce, I. C. (2014). The effects of HCN and KLT ion channels on adaptation and refractoriness in a stochastic auditory nerve model. *IEEE Transactions on Biomedical Engineering*, 61(11):2749–2759.

Nogueira, W. and Ashida, G. (2018). Development of a Parametric Model of the Electrically Stimulated Auditory Nerve. *Springer*, 84.

O'Brien, G. E. and Rubinstein, J. T. (2016). The development of biophysical models of the electrically stimulated auditory nerve: Single-node and cable models. *Network: Computation in Neural Systems*, 27(2-3):135–156.

Paintal, A. S. (1965). Effects of temperature on conduction in single vagal and saphenous myelinated nerve fibres of the cat. *Journal of Neurophysiology*, (1942):20–49.

Paintal, A. S. (1966). The influence of diameter of medullated nerve fibres of cats on the rising and falling phases of the spike and its recovery. *Journal of Physiology*, pages 791–811.

Ranck, J. B. J. (1975). Which elements are excited in electrical stimulation of mammalian central nervous system. *Brain Research*, 98.

Rattay, F. and Aberham, M. (1993). Modeling Axon Membranes for Funtional Electrical Stimulation. *IEEE transactions on biomedical engineering*, 40(12):1201–1209.

Rattay, F., Leao, R. N., and Felix, H. (2001). A model of the electrically excited human cochlear neuron I. Contribution of neural substructures to the generation and propagation of spikes. *Hearing Research*, 153(1-2):64–79.

Reid, G., Scholz, A., Bostock, H., and Vogel, W. (1999). Human axons contain at least five types of voltage-dependent potassium channel. *Journal of Physiology*, 518(3):681–696.

Roper, B. Y. J. and Schwarz, J. R. (2000). Heterogeneous distribution of fast and slow potassium channels in myelinated rat nerve fibers. *Journal of Physiology*, (1989):93–110.

Rubinstein, J. T. (1995). Threshold fluctuations in an N sodium channel model of the node of Ranvier. *Biophysical Journal*, 68(3):779–785.

Rubinstein, J. T. (2004). How cochlear implants encode speech. *Current Opinion in Otolaryngology and Head and Neck Surgery*, 12(5):444–448.

Safronov, B. Y. B. V., Kampe, K., and Vogel, W. (1993). Single voltage-dependent potassium channels in rat peripheral nerve membrane. *Journal of Physiology*, (1993):675–691.

Schmidt Clay, K. M. and Brown, C. J. (2007). Adaptation of the Electrically Evoked Compound Action Potential (ECAP) Recorded from Nucleus CI24 Cochlear Implant Users. *Ear & Hearing*.

Scholz, A., Reid, G., Vogel, W., and Bostock, H. (1993). Ion channels in human axons. *Journal of Neurophysiology*.

Schwarz, J. R. and Eikhof, G. (1987). Na currents and action potentials in rat myelinated nerve fibres at 20 and 37 C. *European Journal of Physiology*, (1987):569–577.

Smit, J. E., Hanekom, T., and Hanekom, J. J. (2009). Modelled temperature-dependent excitability behaviour of a generalised human peripheral sensory nerve fibre. *Biological Cybernetics*, 101(2):115–130.

Smit, J. E., Hanekom, T., van Wieringen, A., Wouters, J., and Hanekom, J. J. (2010). Threshold predictions of different pulse shapes using a human auditory nerve fibre model containing persistent sodium and slow potassium currents. *Hearing Research*, 269(1-2):12–22.

Stypulkowski, P. H. and Van den Honert, C. (1984). Physiological properties of the electrically stimulated auditory nerve. I. Compound action potential recordings. *Hear Res*, 14(3):205–223.

Sweeney, J. D., Mortimer, J. T., and Durand, D. M. (1987). Modeling of mammalian myelinated nerve for functional neuromuscular stimulation. *IEEE 9th Annual Conference of the Engineering in Medicine and Biology Society*, (January 1987):1577–1578.

Takanen, M., Bruce, I. C., and Seeber, B. U. (2016). Phenomenological modelling of electrically stimulated auditory nerve fibers: A review. *Network: Computation in Neural Systems*, 27(2-3):157–185.

Tasaki, I. (1955). New Measurements of the Capacity and the Resistance of the Myelin Sheath and the Nodal Membrane of the Isolated Frog Nerve Fiber.

Van den Honert, C. and Stypulkowski, P. H. (1984). Physiological properties of the electrically stimulated auditory nerve. II. Single fiber recordings. *Hear Research*, 14(3):205–223.

van Gendt, M. J., Briaire, J. J., Kalkman, R. K., and Frijns, J. H. (2016). A fast, stochastic, and adaptive model of auditory nerve responses to cochlear implant stimulation. *Hearing Research*, 341:130–143.

Verveen, A. A. (1960). On the fluctuation of threshold of the nerve fibre. *Structure and function of the cerebral cortex*, pages 282–288.

Verveen, A. A. and Derksen, H. E. (1968). Fluctuation Phenomena in Nerve Membrane. *Proceedings of the IEEE*, 56(6):906–916.

Wesselink, W. A., Holsheimer, J., and Boom, H. B. (1999). A model of the electrical behaviour of myelinated sensory nerve fibres based on human data. *Med.Biol.Eng Comput.*, 37(0140-0118 (Print)):228–235.

Westerman, L. A. and Smith, R. L. (1984). Rapid and short-term adaptation in auditory nerve responses. *Hearing Research*, 15:249–260.

Woo, J., Miller, C., and Abbas, P. (2009). Biophysical Model of an Auditory Nerve Fiber With a Novel Adaptation Component. *IEEE Transactions on Biomedical Engineering*, 56(9):2177–2180.

Woo, J., Miller, C. A., and Abbas, P. J. (2010). The dependence of auditory nerve rate adaptation on electric stimulus parameters, electrode position, and fiber diameter: A computer model study. *JARO - Journal of the Association for Research in Otolaryngology*, 11(2):283–296.

Yi, E., Roux, I., and Glowatzki, E. (2010). Dendritic HCN Channels Shape Excitatory Postsynaptic Potentials at the Inner Hair Cell Afferent Synapse in the Mammalian Cochlea. *Journal of Neurophysiology*, 103(5):2532–2543.

Zhang, F., Miller, C. A., Robinson, B. K., Abbas, P. J., and Hu, N. (2007). Changes across time in spike rate and spike amplitude of auditory nerve fibers stimulated by electric pulse trains. *JARO - Journal of the Association for Research in Otolaryngology*, 8(3):356–372.

Zhou, N., Kraft, C. T., Colesa, D. J., and Pfingst, B. E. (2015). Integration of Pulse Trains in Humans and Guinea Pigs with Cochlear Implants. 534:523–534.

Erklärung der Selbstständigkeit

Hiermit versichere ich, die vorliegende Arbeit selbstständig verfasst und keine anderen als die angegebenen Quellen und Hilfsmittel benutzt sowie die Zitate deutlich kenntlich gemacht zu haben.

....

Ort, Datum Richard Bachmaier